

1 **Augmentation of WRF-Hydro to Simulate Overland Flow- and**
2 **Streamflow-Generated Debris Flow Susceptibility in Burn Scars**

3
4 **Chuxuan Li¹, Alexander L. Handwerger^{2,3}, Jiali Wang⁴, Wei Yu^{5,6}, Xiang Li⁷, Noah J.**
5 **Finnegan⁸, Yingying Xie^{9,10}, Giuseppe Buscarnera⁷, and Daniel E. Horton¹**

6 ¹ Department of Earth and Planetary Sciences, Northwestern University, Evanston, IL, 60208, USA

7 ² Joint Institute for Regional Earth System Science and Engineering, University of California, Los Angeles,
8 CA, 90095, USA

9 ³ Jet Propulsion Laboratory, California Institute of Technology, Pasadena, CA, 91109, USA

10 ⁴ Environmental Science Division, Argonne National Laboratory, Lemont, IL, 60439, USA

11 ⁵ Cooperative Institute for Research in Environmental Sciences, University of Colorado Boulder, CO,
12 80309, USA

13 ⁶ NOAA/Global Systems Laboratory, 325 Broadway Boulder, Denver, CO, 80305-3328, USA

14 ⁷ Department of Civil and Environmental Engineering, Northwestern University, Evanston, IL, 60208, USA

15 ⁸ Department of Earth and Planetary Sciences, University of California Santa Cruz, Santa Cruz, CA, 95064,
16 USA

17 ⁹ Program in Environmental Sciences, Northwestern University, 2145 Sheridan Road, Evanston, IL, 60208,
18 USA

19 ¹⁰ Department of Biological Sciences, Purdue University, 915 W State St, West Lafayette, IN 47907, USA

20
21 *Correspondence to:* Chuxuan Li (chuxuanli2020@u.northwestern.edu)

29 **Abstract**

30 In steep wildfire-burned terrains, intense rainfall can produce large ~~volumes of~~ runoff that can
31 trigger highly destructive debris flows. However, the ability to accurately characterize and forecast
32 debris-flow susceptibility in burned terrains using physics-based tools remains limited. Here, we
33 augment the Weather Research and Forecasting Hydrological modeling system (WRF-Hydro) to
34 simulate both overland and channelized flows and assess postfire debris flow susceptibility over a
35 regional domain. We perform hindcast simulations using high-resolution weather radar-derived
36 precipitation and reanalysis data to drive non-burned baseline and burn scar sensitivity
37 experiments. Our simulations focus on January 2021 when an atmospheric river triggered
38 numerous debris flows within a wildfire burn scar in Big Sur – one of which destroyed California’s
39 famous Highway 1. Compared to the baseline, our burn scar simulation yields dramatic increases
40 in total and peak discharge, and shorter lags between rainfall onset and peak discharge, consistent
41 with streamflow observations at nearby U.S. Geological Survey (USGS) streamflow gage sites.
42 For the 404 catchments located in the simulated burn scar area, median catchment-area normalized
43 peak discharge ~~volume~~ increases ~~nine-fold~~ by ~450% compared to the baseline. Catchments with
44 anomalously high catchment-area normalized peak discharge ~~volumes~~ correspond well with post-
45 event field-based and remotely-sensed debris flow observations. We suggest that our regional post-
46 fire debris flow susceptibility analysis demonstrates WRF-Hydro as a compelling new physics-
47 based tool whose utility could be further extended via coupling to sediment erosion and transport
48 models and/or ensemble-based operational weather forecasts. Given the high-fidelity performance
49 of our augmented version of WRF-Hydro, as well as its potential usage in probabilistic hazard
50 forecasts, we argue for its continued development and application in post-fire hydrologic and
51 natural hazard assessments.

52

53 **Short Summary**

54 In January 2021 a storm triggered numerous debris flows in a wildfire burn scar, ~~in~~ California. We
55 use a hydrologic model to assess debris flow susceptibility in pre-fire and postfire scenarios.
56 Compared to pre-fire conditions, postfire ~~simulation yields~~ conditions yield dramatic increases in
57 ~~total and~~ peak water discharge, substantially increasing debris flow susceptibility. Our work
58 ~~proves~~ highlights the ~~3-D~~ hydrologic ~~models'~~ model's utility ~~to investigate~~ in investigating and
59 potentially ~~forecast~~ forecasting postfire debris ~~flow susceptibility~~ flows at regional scales.

60 **1 Introduction**

61 Following intense rainfall, areas with wildfire burn scars are more prone to flash flooding (Neary
62 et al., 2003; Bart & Hope 2010; Bart 2016) and runoff-generated debris flows than unburned areas
63 (Ice et al., 2004; Shakesby & Doerr, 2006; Moody et al., 2013). After wildfire, reduced tree canopy
64 interception, decreased soil infiltration due to soil-sealing effects (Larsen et al., 2009), and

65 increased soil water repellency – especially in hyper-arid environments (Dekker & Ritsema, 1994;
66 Doerr & Thomas, 2000; MacDonald & Huffman, 2004) – increases excess surface water, and on
67 sloped terrains leads to overland flow (Shakesby & Doerr, 2006; Stoof et al., 2012). As water
68 moves down hillslopes and erosion adds sediment to water-dominated flows, clear water floods
69 can transition to turbulent and potentially destructive debris flows (Meyer & Wells, 1997; Cannon
70 et al., 2001, 2003; Santi et al., 2008). In contrast to debris flows initiated by shallow landslides,
71 this rainfall-runoff process has been identified as the major cause for postfire debris flows in the
72 western U.S. (Cannon, 2001; Cannon et al., 2003, 2008; Kean et al., 2011; Parise & Cannon, 2012;
73 Nyman et al., 2015), and in other regions ~~with Mediterranean climates that are particularly~~
74 ~~susceptible to wildfires and subsequent heavy precipitation~~ (Bisson et al., 2005; Mitsopoulos &
75 Mironidis, 2006; Rosso et al., 2007; Parise & Cannon, 2008, 2009). ~~In California, because climate~~
76 ~~change is projected to~~

77 ~~On the U.S. west coast, atmospheric rivers (ARs) are the dominant synoptic weather systems~~
78 ~~responsible for producing postfire debris flows (Barth et al., 2017; Oakley et al., 2017, 2018;~~
79 ~~Young et al., 2017). ARs are long filament-like bands of elevated water vapor within the lower~~
80 ~~troposphere that often form over ocean basins. They are responsible for over 90% of poleward~~
81 ~~water vapor transport (Zhu & Newell, 1998) and often result in heavy precipitation upon landfall,~~
82 ~~particularly with orographic uplift (Ralph et al., 2004; Neiman et al., 2008). It is reported that 30–~~
83 ~~50% of annual precipitation and 60%–100% of extreme precipitation along the U.S. west coast is~~
84 ~~the result of ARs (Collow et al., 2020; Eldardiry et al., 2019; Hecht & Cordeira, 2017). In~~
85 ~~California, anthropogenic climate change is projected to increase AR intensity (Huang et al.,~~
86 ~~2020a, 2020b), increase the intensity and frequency of wet-season precipitation (Polade et al.,~~
87 ~~2017; Swain et al., 2018), increase wildfire potential (Brown et al., 2020; Swain, 2021), and extend~~
88 ~~the wildfire season (Goss et al., 2020). As such, the occurrence and intensity of postfire debris~~
89 ~~flows are likely to increase as the effects of anthropogenic climate change persist (Cannon &~~
90 ~~DeGraff, 2009; Kean & Staley, 2021; Oakley, 2021).~~

91 Due to this increasing threat, the development of tools to assess postfire debris flow susceptibility
92 and hazards is critical. However, due to long-standing terminology ambiguity in the natural hazard
93 community (Reichenbach et al., 2018), we first begin with a definition of terms. In this study we
94 demonstrate the use of a new physics-based tool to map postfire debris flow susceptibility at
95 regional scales. We follow the guidance of [Reichenbach et al., (2018) & references therein] and
96 define *susceptibility* as the likelihood of debris flow occurrence in an area, and *hazard* as the
97 probability of debris flow occurrence of a given magnitude within a specified area and period of
98 time. In other words, debris flow susceptibility ~~does not estimate~~ ~~neither simulates debris flow~~
99 ~~dynamics such as initiation nor estimates~~ debris flow size or ~~considers~~ ~~considers~~ the timing or
100 frequency of the debris flow occurrence. Rather, it focuses on locating areas prone to debris flows
101 considering local environmental factors (Brabb 1985; Guzzetti et al., 2005).

102 Heuristic, deterministic, statistical approaches, and coupled deterministic and statistical models
103 have previously been employed to assess landslide susceptibility (Dahal et al., 2008; Regmi et al.,

- Formatted: Font color: Auto
- Formatted: Font color: Auto
- Formatted: Font color: Auto
- Formatted: Font color: Auto
- Formatted: Font color: Auto
- Formatted: Font color: Auto
- Formatted: Font color: Auto
- Formatted: Font color: Auto
- Formatted: Font color: Auto

104 2010; Park et al., 2016; Reichenbach et al., 2018). For postfire debris flow susceptibility or hazard
105 assessment, however, the use of deterministic models is limited. In contrast, statistical approaches
106 are commonly used in both research and operational settings (Cannon et al., 2010; Friedel 2011a,
107 2011b; Gardner et al., 2014; Staley et al., 2016; Nikolopoulos et al., 2018; Cui et al., 2019). For
108 example, rainfall intensity-duration (ID) thresholds are one of the simplest-to-implement and most
109 widely used statistical methods for mapping rainfall-induced landslide susceptibility including
110 postfire debris flows (Cannon et al., 2011; Staley et al., 2017). In addition, the U.S. Geological
111 Survey (USGS) currently employs a statistical approach in their Emergency Assessment of
112 Postfire Debris-flow Hazards that consists of a logistic regression model to predict the likelihood
113 of post-wildfire debris flows (e.g., Cannon et al., 2010; Staley et al., 2016), and a multiple linear
114 regression model to predict debris flow volumes (Gartner et al., 2014). Machine-learning
115 techniques such as self-organizing maps, genetic programming, and a random forest algorithm
116 have also been used to predict postfire debris flows in the western U.S. (Friedel 2011a, 2011b;
117 Nikolopoulos et al., 2018). In general, statistical approaches are useful for identifying and
118 characterizing relationships amongst contributing environmental factors and are widely used due
119 to their low computational costs and the potential for rapid assessment. Despite the utility and
120 advantages of data-driven hazard prediction approaches over regional domains, these techniques
121 (1) do not simulate the underlying physics, (2) often require large amount of historical observation
122 data that may not be readily available, and (3) result in models that are often only applicable to
123 specific locales. These limitations inhibit their utility in ~~developing a better process based~~
124 ~~understanding of postfire~~ debris flow ~~mechanics~~susceptibility assessment from a physics-based
125 ~~perspective~~, limit their applicability in climatological and geographic settings different than their
126 training sites, and limit their use in non-stationary conditions (e.g., under changing climatic
127 conditions).

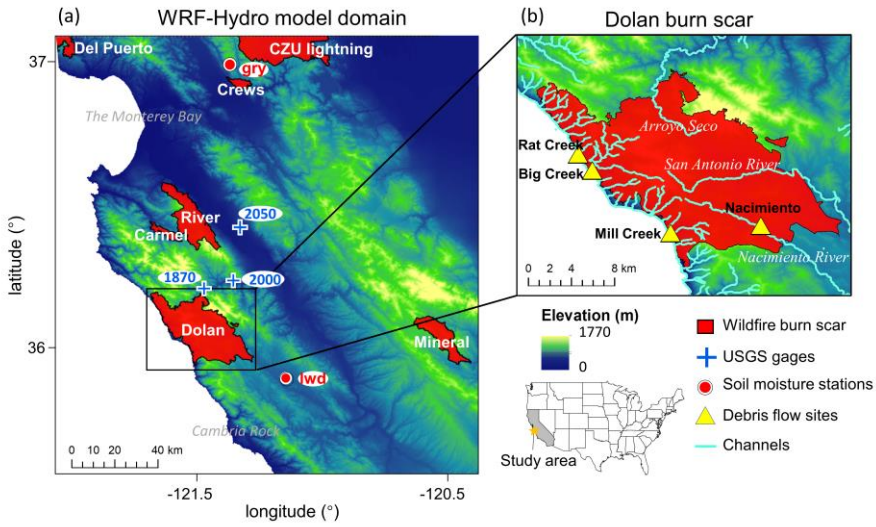
128 In contrast, physics-based models that simulate spatially-explicit hydrologic and mass wastage
129 processes are well-suited for ~~meehanistic~~sensitivity analyses in diverse settings. However, studies
130 employing deterministic process-based models have tended to focus on ~~modeling~~rainfall-induced
131 shallow landslides (Crosta & Frattini, 2003; Claessens et al., 2007) or landslide-induced debris
132 flows (e.g., Iverson & George, 2014; George & Iverson, 2014), rather than on runoff-generated
133 debris flows which are more common in postfire areas (Cannon et al., 2001, 2003; Santi et al.,
134 2008). Studies that have investigated postfire hydrologic responses using physics-based models
135 have largely focused on ~~mechanistic studies such as~~ short-term responses at high spatiotemporal
136 resolutions (Rengers et al., 2016; McGuire et al., 2016, 2017) or long-term runoff responses at
137 coarse temporal resolutions (McMichael & Hope, 2007; Rulli & Rosso, 2007) in individual
138 catchments ~~rather than assessing susceptibility over regional domains.~~ For example, process-
139 based models have employed shallow water equations to ~~better~~ understand the triggering (McGuire
140 et al., 2017; Tang et al., 2019a, 2019b) and ~~sediment~~ transport mechanisms (McGuire et al., 2016)
141 of postfire debris flows ~~in single catchments (McGuire et al., 2016, 2017) and to investigate as well~~
142 ~~as~~ the timing of postfire debris flows ~~in three separate catchments (Rengers et al., 2016), the latter).~~
143 ~~The numerical models employed by these studies are used to simulate debris flow dynamics rather~~

Formatted: Font color: Black

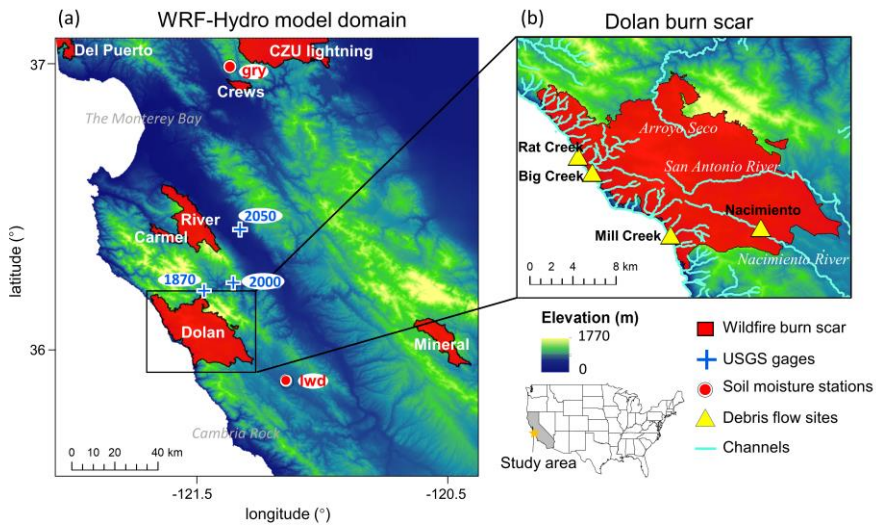
144 [than assess susceptibility over regional domains, as such they focus on individual catchments \(with](#)
145 [drainage areas of which also assessed the efficacy of a simplified kinematic wave approach.~1](#)
146 [km²\) with very high spatiotemporal resolutions \(Rengers et al., 2016; McGuire et al., 2016, 2017;](#)
147 [Tang et al., 2019a, 2019b\).](#) In addition to individual catchment applications, process-based models
148 often adopt simplifications that can limit effective prediction and hypothesis testing to overcome
149 computational limits. For example, the kinematic runoff and erosion model (KINEROS2)
150 simplifies drainage basins into 1-dimensional channels and hillslope patches (Canfield et al., 2005;
151 Goodrich et al., 2012; Sidman et al., 2016), and the Hydrologic Modeling System (HEC-HMS)
152 uses an empirically-based curve number method to estimate saturation excess water (Cyzdik et al.,
153 2009), which cannot resolve infiltration excess overland flow, a critical process in burn scars (Chen
154 et al., 2013).

155 Given the current state of debris flow susceptibility assessment and prediction in previously burned
156 terrains, in addition to the growing influence of anthropogenic climate change on wildfire and
157 extreme precipitation, development of physics-based susceptibility mapping tools that can be used
158 in both hindcast investigations and forecasting applications is needed. Furthermore, due to the
159 diverse morphology and often large spatial scales of precipitation events and their interactions with
160 geographically distributed wildfire burn scars, development of tools that can assess susceptibility
161 over regional domains, particularly in operational forecasting applications, is critical. Here, to
162 advance the field of burn scar debris flow susceptibility assessment, we explore the use of the
163 physics-based and fully-distributed Weather Research and Forecasting Hydrological modeling
164 system version 5.1.1 (WRF-Hydro). WRF-Hydro is an open-source community model developed
165 by the National Center for Atmospheric Research (NCAR). It is the core of the National Oceanic
166 and Atmospheric Administration's (NOAA) National Water Model forecasting system and has
167 been used extensively to study channelized flows over regional domains (e.g., Wang et al., 2019;
168 Lahmers et al., 2020). Here, we modify WRF-Hydro to output high temporal resolution fine-scale
169 (100 m) debris flow-relevant overland flow; a process computed using a fully unsteady, explicit,
170 finite difference diffusive wave formulation. Previous efforts, employing shallow water equations,
171 diffusive, kinematic, and diffusive-kinematic wave models, have demonstrated that water-only
172 models can provide critical insights on runoff-driven debris [flowflows](#) (Arattano & Savage, 1994;
173 [ArratanoArattano](#) & Franzi, 2010; Di Cristo et al., 2021), even in burned watersheds (Rengers et
174 al., 2016; McGuire & Youberg, 2020).

175 To test and demonstrate the utility of WRF-Hydro in debris flow studies, we investigate the
176 January 2021 debris flow events within the Dolan burn scar on the Big Sur coast of central
177 California (Fig. 1a–b). We first identify multiple debris flow sites using optical and radar remote
178 sensing data and field investigations. We then calibrate WRF-Hydro against ground-based soil
179 moisture and streamflow observations and use it to study the effects of burn scars on debris flow
180 hydrology and susceptibility. The paper is organized as follows. Section 2 describes the
181 identification approach and geologic setting of debris flows. Section 3 presents a description of
182 WRF-Hydro. Section 4 describes the simulation, calibration, and validation of WRF-Hydro.
183 Section 5 presents the results. Section 6 discusses the results and Sect. 7 provides a conclusion.



184



185

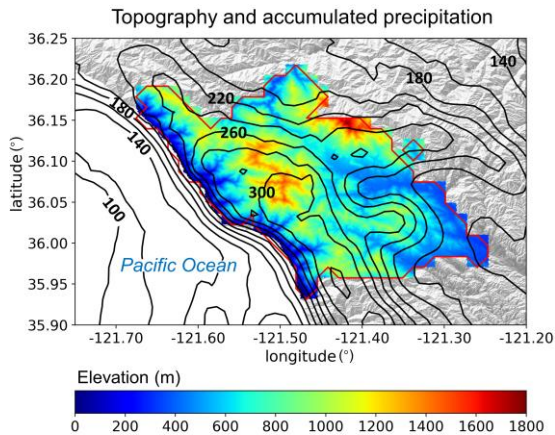
186 **Fig. 1|** WRF-Hydro model domain and Dolan burn scar. (a) WRF-Hydro model domain depicting
187 topography, 2020 wildfire season burn scars, and PSL soil moisture and USGS stream gage
188 observing sites. The black rectangle outlines (b) the Dolan burn scar inset, in which debris flow
189 locations and major streams are marked and labeled. The location of the study area is shown in the
190 embedded U.S. map with the state of California shaded in grey.

191

192 2 Study domain and debris flow identification methodology

193 The Dolan wildfire burned from August 18th till December 31st, 2020. 55% of areas within the fire
194 perimeter were burned at moderate-to-high severity (Burned Area Emergency Response, 2020).
195 After the fire, USGS Emergency Assessment of Postfire Debris-flow Hazards produced a debris
196 flow hazard assessment using a design storm based statistical model (USGS, 2020). On January
197 27–29, 2021, an [atmospheric river \(AR\)](#) made landfall on the Big Sur coast, bringing more than
198 300 mm of rainfall to California’s Coast Ranges (Fig. 2), with a peak rainfall rate of 24 mm h⁻¹.
199 [\[calculated with Multi-Radar/Multi-Sensor System \(MRMS\) precipitation; Zhang et al., 2011,](#)
200 [2014, 2016\]](#). During the AR event, a section of California State Highway 1 (CA1) at Rat Creek
201 was destroyed by a debris flow. CA1 was subsequently closed for three months and rebuilt at a
202 cost of ~\$11.5M (Los Angeles Times, 2021).

203



204

205

206 **Fig. 2|** The topography ([m](#); shading; [m](#)) and MRMS accumulated precipitation ([mm](#); contour lines;
207 [mm](#)) during the AR event from January 27th 00:00 to 29th 23:00 in the Dolan burn scar. Contour

208 line interval for accumulated precipitation is 20 mm, and lines of 100, 140, 180, 220, 260, and 300
209 mm are labeled. The red polygon outlines the perimeter of the Dolan burn scar.

210
211

212 **2.1 Debris flow identification from remote sensing and field work**

213 In addition to the Rat Creek debris flow, which made national news (Los Angeles Times, 2021),
214 we identified three other debris flows using a combination of field investigation, and open access
215 satellite optical and synthetic aperture radar (SAR) images (Fig. 3 and Fig. B1).

216 We examined relative differences in normalized difference vegetation index (rdNDVI) defined by
217 (Scheip & Wegmann, 2021):

$$218 \quad rdNDVI = \frac{NDVI_{post} - NDVI_{pre}}{\sqrt{NDVI_{pre} + NDVI_{post}}} \times 100 \quad (1)$$

219 where $NDVI_{pre}$ and $NDVI_{post}$ are the pre- and post-event normalized difference vegetation index
220 (NDVI) images computed following:

$$221 \quad NDVI = \frac{NIR - Red}{NIR + Red} \quad (2)$$

222 where NIR is the near-infrared response and Red is the visible red response. rdNDVI was calculated
223 from 10-m Sentinel-2 satellite data using the HazMapper v1.0 Google Earth Engine application
224 (Scheip & Wegmann, 2021). HazMapper requires selection of an event date, pre-event window
225 (months), post-event window (months), max cloud cover (%) and slope threshold ($^{\circ}$). These input
226 requirements filter the number of images used to calculate the rdNDVI. We set the event date to
227 January 27th, 2021 and used a 3 month pre- and post-event window with 0% max cloud cover and
228 a 0° slope threshold to identify vegetation loss associated with the debris flows. We then created
229 a binary map to highlight debris flows (and other vegetation loss) pixels above a rdNDVI
230 vegetation loss threshold. We removed all pixels with $rdNDVI > -10$.

231 Lastly, we searched for debris flows (and other ground surface deformation) by examining SAR
232 backscatter change with data acquired by the 10-m Copernicus Sentinel-1 (S1) satellites [see full
233 description in Handwerger et al. (2022)]. We measured the change in SAR backscatter by using
234 the log ratio approach, defined as

$$235 \quad I_{ratio} = 10 \times \log_{10} \left(\frac{\sigma_{pre}^0}{\sigma_{post}^0} \right) \quad (3)$$

236 where σ_{pre}^0 is a pre-event image stack (defined as the temporal median) of SAR backscatter and
237 σ_{post}^0 is a post-event image stack. Similar to the HazMapper method, our approach requires
238 selection of an event date, pre-event window (months), post-event window (months) and slope
239 threshold ($^{\circ}$). No cloud-cover threshold is needed since SAR penetrates clouds. We used a 3 month
240 pre- and post-event window and 0° slope threshold to identify ground surface changes associated

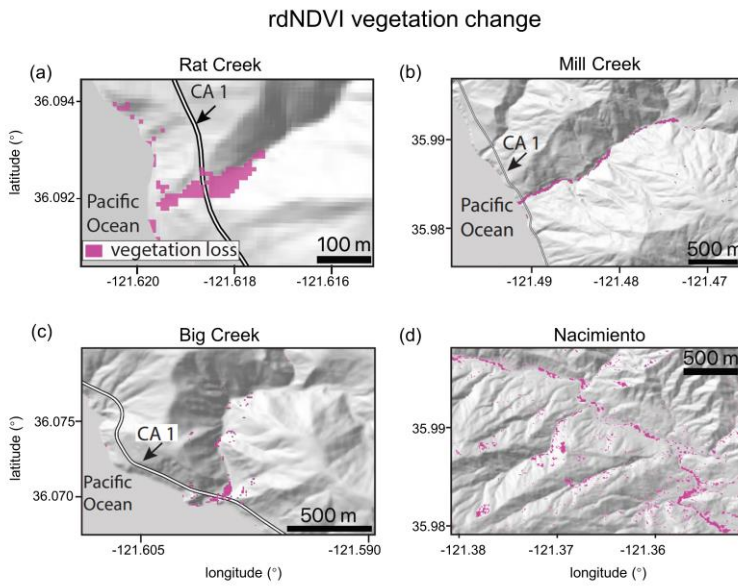
Formatted: Not Highlight

Formatted: Not Highlight

241 with the debris flows. We then created a binary map to highlight debris flows by removing all
242 pixels with $I_{ratio} < 99^{\text{th}}$ percentile value [i.e., threshold suggested by Handwerger et al. (2022)].

243 Identified debris flow source areas and deposition sites were confirmed by field investigation (N.J.
244 Finnegan) and named after the locations where they deposited (i.e., Big Creek, Mill Creek, and
245 Nacimiento).

246



247
248 **Fig. 3** Identified debris flow sites using rdNDVI vegetation change within the Dolan burn scar.
249 We convert the rdNDVI data into a binary map by setting a threshold value, which yields only the
250 likely debris flow locations and drape these maps over a topographic hillshade. (a)–(d) Sentinel-2
251 rdNDVI vegetation change at (a) Rat Creek, (b) Mill Creek, (c) Big Creek, and (d) the Nacimiento
252 River.

253

254 2.2 Debris flow geologic setting

255 According to the USGS National Elevation Dataset 30-m digital elevation model (DEM), the Rat
256 Creek debris flow sits at the base of a 1st order catchment with a drainage area of 2.23 km². Mill
257 Creek, Big Creek, and Nacimiento debris flows were initiated within extremely steep, intensely
258 burned, 1st order catchments, but were deposited in 2nd, 3rd, and 3rd Strahler stream order channels,

259 respectively. All four debris flows were channelized. Rat Creek, Mill Creek, and Big Creek debris
260 flow deposition sites have elevations ranging from 20–60 m, while Nacimiento debris flow
261 deposited at an elevation of ~440 m above sea level. We calculate catchment slopes using the DEM
262 and the slope calculation function in ArcMap. The average slope of the catchments containing Rat
263 Creek and Mill Creek debris flow deposition sites is ~25°. The average catchment slope of Big
264 Creek deposition site is ~28° and Nacimiento is ~21°. For debris flow source areas, the average
265 and maximum slopes of Mill Creek are 23° and 39°, 21° and 43° for Big Creek, and 24° and 41°
266 for Nacimiento. According to the Soil Survey Geographic Database and California geologic map
267 data, surface soils at the three coastal debris flow sites (i.e., Rat Creek, Mill Creek, and Big Creek)
268 are texturally classified as loam with underlying Franciscan Complex sedimentary rocks of
269 Jurassic to Cretaceous age. Soil at Nacimiento is classified as sandy loam with underlying Upper
270 Cretaceous and Paleocene marine sedimentary rocks from the Dip Creek Formation, Asuncion
271 Group, Shut-In Formation, Italian Flat Formation, Steve Creek Formation, and El Piojo Formation.
272 Mill Creek, Big Creek, and Nacimiento were relatively large debris flows with runout lengths
273 between ~2–5 km, while Rat Creek occurred in a smaller catchment and had a runout length of
274 ~300 m. The difference in runout length and debris flow size is primarily controlled by upstream
275 catchment size, however for the three coastal debris flow events at Rat Creek, Big Creek, and Mill
276 Creek, also constrained by the downslope ocean. We note that there were likely more debris flows
277 triggered during the AR event. The four debris flow events highlighted here were identified during
278 brief post-event field excursions due to their intersection with major roadways. Given that our
279 primary goal here is to demonstrate the utility of WRF-Hydro – a comprehensive catalogue of
280 debris flows is beyond the scope of this study, although underway by other researchers (Cavagnaro
281 et al., 2021).

282 **3 WRF-Hydro**

283 **3.1 Model description**

284 WRF-Hydro is an open-source physics-based community model that simulates land surface
285 hydrologic processes. It includes the Noah-Multiparameterization (Noah-MP) land surface model
286 (LSM; Niu et al., 2011), terrain routing module, channel routing module, and a conceptual
287 baseflow bucket model. The Noah-MP LSM is a 1-dimensional column model that calculates
288 vertical energy fluxes (i.e., sensible and latent heat, net radiation), moisture (i.e., canopy
289 interception, infiltration, infiltration excess, deep percolation), and soil thermal and moisture states
290 on the LSM grid (1 km in our application). The infiltration excess, ponded water depth, and soil
291 moisture are then disaggregated using a time-step weighted method (Gochis & Chen, 2003) and
292 sent to the terrain routing module which simulates subsurface and overland flows on a finer terrain
293 routing grid (100 m in our application). According to the mass balance, local infiltration excess,
294 overland flow, and exfiltration from baseflow contribute to the surface head which flows into river
295 channels if defined retention depth is exceeded. The channel routing module then calculates
296 channelized flows assuming a trapezoidal channel shape (Fig. B2). Parameters related to the

297 trapezoidal channel, such as channel bottom width (B_w), Manning's roughness coefficient (n), and
 298 channel side slope (z) are functions of channel stream order (Fig. B3 and Table B1). Channelized
 299 streamflow is computed at spatial resolutions ranging from 1.5 m to 100 m depending on the
 300 channel stream order (Table B1). Computed streamflow is then output on the 100-m grid.
 301 Equations used to compute infiltration excess, overland flow, and channelized flow are provided
 302 in Sect. 3.3 and 3.4.

303 By default, WRF-Hydro uses Moderate Resolution Imaging Spectroradiometer (MODIS)
 304 Modified International Geosphere-Biosphere Program (IGBP) 20-category land cover product as
 305 land cover (Fig. B4) and 1-km Natural Resources Conservation Service State Soil Geographic
 306 (STATSGO) database for soil type classification (Fig. B5; Miller & White, 1998). Land surface
 307 properties including canopy height (HVT), maximum carboxylation rate (VCMX25), and overland
 308 flow roughness (OV_ROUGH2D) are functions of land cover type (Table B2 & Fig. B4). Default
 309 soil hydraulic parameters in WRF-Hydro (i.e., soil porosity, grain size distribution index, and
 310 saturated hydraulic conductivity) are based on Cosby et al.'s (1984) soil analysis (Table B3) and
 311 are used to map onto the STATSGO 16 soil texture types (Fig. B5).

312

313 3.2 Meteorological forcing files

314 WRF-Hydro is used in a standalone mode (i.e., it is not interactively coupled with the atmospheric
 315 component of WRF), but rather is forced with a combination of Phase 2 North American Land
 316 Data Assimilation System (NLDAS-2) meteorological data and ~~Multi-Radar/Multi-Sensor~~
 317 ~~System (MRMS)~~ radar-only quantitative precipitation (Zhang et al., 2011, 2014, 2016). A
 318 description of the MRMS dataset and uncertainties therein can be found in Appendix A. NLDAS-
 319 2 provides hourly forcing data including incoming shortwave and longwave radiation, 2-m specific
 320 humidity and air temperature, surface pressure, and 10-m wind speed at 1/8-degree spatial
 321 resolution. MRMS provides hourly precipitation rates at 1-km resolution.

322

323 3.3 Overland flow routing and output

324 The Noah-MP LSM calculates rate of infiltration excess following Chen & Dudhia (2001):

325

$$326 \quad \frac{\partial h}{\partial t} = \frac{\partial P_d}{\partial t} \left\{ 1 - \frac{[\sum_{i=1}^4 \Delta D_i (\theta_s - \theta_i)] \left[1 - \exp \left(-k \frac{K_s}{K_{ref}} \delta_t \right) \right]}{P_d + [\sum_{i=1}^4 \Delta D_i (\theta_s - \theta_i)] \left[1 - \exp \left(-k \frac{K_s}{K_{ref}} \delta_t \right) \right]} \right\} \quad (4)$$

327

328 where h (m) is the surface water depth and t is the time. P_d (m) is the precipitation not intercepted
 329 by the canopy; ΔD_i (m) is the depth of soil layer i ; θ_i is the soil moisture in soil layer i ; θ_s is the
 330 soil porosity; K_s (m s^{-1}) is the saturated hydraulic conductivity; K_{ref} is $2 \times 10^{-6} \text{ m s}^{-1}$ which

Formatted: Not Highlight

331 represents the saturated hydraulic conductivity of the silty-clay-loam soil texture chosen as a
 332 reference; δ_t (s) is the model time step; and k which is equal to 3.0 is the runoff-infiltration
 333 partitioning parameter [the same as kdt_{ref} in Chen & Dudhia (2001)].

334

335 Noah-MP passes excess water to the terrain routing module, which simulates overland flow using
 336 a 2-dimensional fully-unsteady, explicit, finite-difference diffusive wave equation adapted from
 337 Julien et al. (1995) and Ogden (1997). In this application, the computation of overland flow is
 338 computed at each 6-s temporal resolution second time step and is archived hourly at 100-m spatial
 339 resolution. The diffusive wave equation is considered improved compared to the traditionally used
 340 kinematic wave formulation in that it accounts for backwater effects and flow over adverse slopes.
 341 The diffusive wave formulation is the simplified form of the Saint Venant equations, i.e.,
 342 continuity and momentum equations for a shallow water wave. The 2-dimensional continuity
 343 equation for a flood wave is:

$$344 \quad \frac{\partial h}{\partial t} + \frac{\partial q_x}{\partial x} + \frac{\partial q_y}{\partial y} = i_e \quad (5)$$

345 where h is the surface flow depth, q_x and q_y are the unit discharges in the x- and y-directions,
 346 respectively, and i_e is the infiltration excess. Manning's equation which considers momentum loss
 347 is used to calculate q . In the x-direction:

$$348 \quad q_x = \alpha_x h^\beta \quad (6)$$

349 Where β is a unit dependent coefficient equal to $\frac{5}{3}$, and

$$350 \quad \alpha_x = \frac{S_{fx}^{1/2}}{n_{ov}} \quad (7)$$

351 where n_{ov} is the tunable overland flow roughness coefficient. The momentum equation in the x-
 352 direction is given by:

$$353 \quad S_{fx} = S_{ox} - \frac{\partial h}{\partial x} \quad (8)$$

354 where S_{fx} is the friction slope, S_{ox} is the terrain slope, and $\frac{\partial h}{\partial x}$ is the change in surface flow depth
 355 in the x-direction.

356 Off-the-shelf, WRF-Hydro does not output overland flow at terrain routing grids (100 m), however
 357 it is computed in the background to determine channelized streamflow. One key advance made in
 358 this work is that we modified WRF-Hydro source code to output overland flow (see the Code
 359 availability statement for the modified source code). Overland flow depth (m) was converted to
 360 overland discharge ($m^3 s^{-1}$) by multiplying flow depth by grid cell area ($10,000 m^2$) and dividing
 361 by the LSM time step (1 h).

362

Formatted: Not Highlight

Formatted: Not Highlight

Formatted: Not Highlight

Formatted: Not Highlight

Formatted: Not Highlight

Formatted: Not Highlight

Formatted: Not Highlight

363 3.4 Channel routing

364 If overland flow intersects grid cells identified as channel grids (2nd Strahler stream order and
365 above; pre-defined by the hydrologically conditioned USGS 30-m DEM), the channel routing
366 module routes the water as channelized streamflow using a 1-dimensional, explicit, variable time-
367 stepping diffusive wave formulation. In this work, the channel routing module calculates
368 streamflow at 6-s temporal resolution and spatial resolutions ranging from 1.5 m to 100 m
369 depending on the channel stream order (Fig. B3 and Table B1). Similarly, the continuity equation
370 for channel routing is given as:

$$371 \quad \frac{\partial A}{\partial t} + \frac{\partial Q}{\partial s} = q_l \quad (9)$$

372 and the momentum equation is given as:

$$373 \quad \frac{\partial Q}{\partial t} + \frac{\partial(\frac{\gamma Q^2}{A})}{\partial s} + gA \frac{\partial H}{\partial s} = -gAS_f \quad (10)$$

374 where s is the streamwise coordinate, H is water surface elevation, A is the flow cross-sectional
375 area calculated as $(B_w + H z)H$ (Fig. B2), q_l is the lateral inflow rate into the channel grid, Q is
376 the flow rate, γ is a momentum correction factor, g is acceleration due to gravity, and S_f is the
377 friction slope computed as:

$$378 \quad S_f = \left(\frac{Q}{K}\right)^2 \quad (11)$$

379 where K is the conveyance computed from the Manning's equation:

$$380 \quad K = \frac{C_m}{n} AR^{2/3} \quad (12)$$

381 where n is the Manning's roughness coefficient, A is the channel cross-sectional area, R is the
382 hydraulic radius (A/P), P is the wetted perimeter, and C_m is a dimensional constant (1.486 for
383 English units or 1.0 for SI units).

384

385 4 Model simulation, calibration, and validation

386 4.1 Model domain

387 The WRF-Hydro model domain spans regions in California including the Coast Ranges, Monterey
388 Bay, and the Central Valley, and covers several burn scars from the 2020 wildfire season (Fig. 1a).
389 Here we focus our analysis on the Dolan burn scar where the hazardous debris flows occurred (Fig.
390 1b).

391 To calibrate and validate WRF-Hydro output, we use soil moisture observations from two Physical
392 Sciences Laboratory (PSL) monitoring stations [i.e., Lockwood (lwd) and Gilroy (gry)] (Fig. 1a).
393 Due to the Mediterranean climate of California, many USGS stream gages experience low or no

Formatted: Not Highlight

394 flow during the dry season. In addition, many gages are under manual regulation to mitigate wet-
395 season flood risks and better distribute water resources. As such, it can be challenging to obtain
396 natural streamflow observations for model calibration. Here, three USGS stream gages [i.e.,
397 Arroyo Seco NR Greenfield, CA (ID 11151870), Arroyo Seco NR Soledad, CA (ID 11152000),
398 and Arroyo Seco BL Reliz C NR Soledad, CA (ID 11152050)] (Fig. 1a) on streams that have
399 measurable flows during our study period and are free of human regulation are used. These gages
400 are located downstream of the Dolan burn scar and hence are useful in calibrating the parameters
401 associated with burn scar effects. The PSL soil moisture observations were recorded at 2-minute
402 intervals and USGS streamflow gage data were recorded at 15-minute intervals, but we perform
403 all observation-model comparisons at hourly-mean resolution.

404
405

406 **4.2 Baseline simulation and soil moisture calibration**

407 WRF-Hydro was initialized with National Centers for Environmental Prediction (NCEP) FNL
408 (Final) Operational Global Analysis data and was run from January 1–31, 2021. We performed the
409 baseline simulation by modifying WRF-Hydro default parameters (Table B3) based on a
410 calibration using soil moisture observations from stations lwd and gry. Neither PSL station is
411 located in a burn scar. Since the baseline simulation includes no postfire characteristics, it can also
412 be regarded as the “pre-fire” scenario. Soil moisture at 10 cm below ground in the baseline
413 simulation was calibrated by performing a domain-wide adjustment of soil porosity and grain size
414 distribution index at the simulation start (Table B3). We then allowed the model to spin up from
415 January 1–10 before using January 11–31 for validation. Using a relatively short spin-up period is
416 justified because prior to the AR event, little rain fell on the Dolan burn scar (i.e., ~400 mm of
417 rainfall fell from June to December 2020). As such, in the months preceding the debris flow events,
418 soil moisture observations indicate already dry conditions prior to our 10 day spin up.

419
420 After calibration, the simulated soil moisture closely mimics ground-based PSL observations (Fig.
421 4). Both the observed magnitude and variability are well captured, with the simulated ± 1 standard
422 deviation envelope largely encompassing PSL observations during the AR. Model performance
423 was evaluated using four quantitative metrics, i.e., correlation coefficient (r), root mean square
424 error (RMSE), mean absolute error (MAE), and Kling-Gupta efficiency (KGE; Gupta et al., 2009;
425 Kling et al., 2012). KGE has previously been used in soil moisture calibration applications (e.g.,
426 Lahmers et al., 2019; Vergopolan et al., 2020) and is computed as follows:

$$427 \quad KGE = 1 - \sqrt{(r - 1)^2 + (\alpha - 1)^2 + (\beta - 1)^2} \quad (13)$$

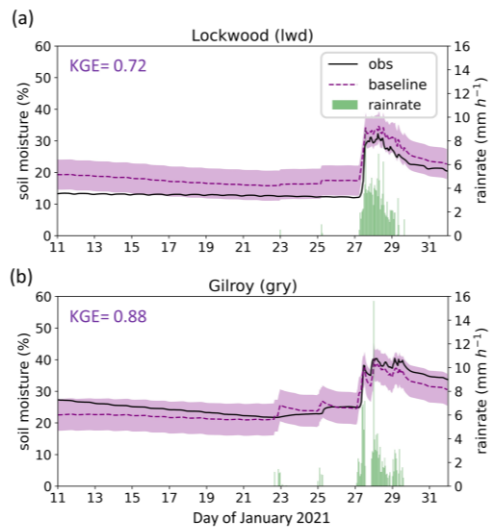
428
429
430 where r is the correlation coefficient between the observation and simulation, α is the ratio of the
431 standard deviation of simulation to the standard deviation of observation, and β is the ratio of the

432 mean of simulation to the mean of observation. KGEs close to 1 indicate a high-level consistency
433 between the simulation and observation, while negative KGEs indicate poor model performance
434 (Andersson et al., 2017; Schönfelder et al., 2017).

435
436 The model's ability to simulate soil moisture substantially improves after calibration (Fig. 4; Table
437 1). KGE values approach 1 (0.72 at lwd and 0.88 at gry), indicating that WRF-Hydro adequately
438 simulates the hydrologic environment and its response to meteorological changes.

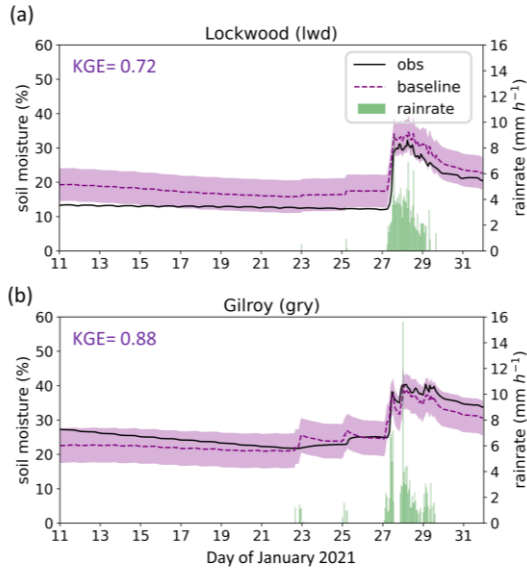
439

MRMS precipitation, observed and simulated soil moisture



440

MRMS precipitation, observed and simulated soil moisture



441
 442 **Fig. 4|** Precipitation, observed and simulated soil moisture at two PSL soil moisture stations.
 443 January 11–31, 2021 MRMS precipitation (mm h^{-1} ; green bars) and observed θ (%) (black line) and
 444 simulated volumetric soil moisture 10 cm below ground in the baseline simulation (%) (purple
 445 dashed line) at PSL sites (a) Lockwood (lwd) and (b) Gilroy (gry). Envelope of purple shading
 446 depicts ± 1 standard deviation of model simulated soil moisture. KGE scores are provided at top
 447 left for each station.

448
 449
 450

451 *Table 1*
 452 *Evaluation metrics of simulated soil moisture and streamflow*

453

Soil moisture (Default / Baseline)				
Station	r	RMSE	MAE	KGE
lwd	0.97 / <u>0.98</u>	7.06 / <u>4.32</u>	5.21 / <u>4.16</u>	0.10 / <u>0.72</u>

gry	0.94 / 0.94	5.19 / <u>2.53</u>	11.12 / <u>2.31</u>	0.80 / <u>0.88</u>
Streamflow (Baseline / Burn scar)				
Station	<i>r</i>	RMSE	MAE	NSE
1870	0.28 / <u>0.93</u>	39.29 / <u>14.69</u>	16.05 / <u>6.14</u>	-0.17 / <u>0.84</u>
2000	0.26 / <u>0.86</u>	51.22 / <u>24.92</u>	20.11 / <u>10.00</u>	-0.15 / <u>0.73</u>
2050	0.25 / <u>0.81</u>	49.96 / <u>27.43</u>	19.64 / <u>11.65</u>	-0.38 / <u>0.53</u>

454
455 **Table 1** | Quantitative evaluation metrics for the simulated soil moisture and streamflow when
456 compared against observations. The metrics include the Pearson correlation coefficient (*r*), root
457 mean square error (RMSE), and mean absolute error (MAE). In addition, the comprehensive
458 metrics Kling-Gupta efficiency (KGE) and Nash-Sutcliffe efficiency (NSE) are used to evaluate
459 model-simulated soil moisture and streamflow, respectively. For soil moisture, the numbers in
460 front of “/” are calculated between the default run (i.e., uncalibrated run) and the observations,
461 whereas the numbers following “/” are the corresponding values in the baseline simulation (the
462 purple dashed line in Fig. 4). For streamflow, the numbers in front of “/” are computed between
463 the baseline run (purple dashed line in Fig. 6) and the observations, while the numbers behind “/”
464 are for burn scar simulation (red line in Fig. 6). If the model performance regarding a certain metric
465 is enhanced in the burn scar simulation, the number after “/” is underlined.
466

467 **4.3 Burn scar simulation and streamflow calibration**

468 To simulate effects of wildfire burn scars on hydrologic processes and debris flow susceptibility,
469 we made two modifications to the baseline simulation soil moisture calibrated model configuration.
470 First, we changed the land cover type within the burn scar perimeter to its nearest LSM analogue,
471 i.e., “barren and sparsely vegetated”. The switch to barren land causes: (1) height of the canopy
472 (HVT) to decrease to 0.5 m; (2) maximum rate of carboxylation at 25°C (VCMX25) to decrease
473 to 0 $\mu\text{mol CO}_2/(\text{m}^2 \cdot \text{s})$; and (3) overland flow roughness coefficient (OV_ROUGH2D) to decrease
474 to 0.035 (Fig. 5a–c) from default values (Fig. B4 and Table B2).

475
476 The second adjustment was to decrease soil infiltration rates within the burn scar perimeter,
477 achieved by reducing soil saturated hydraulic conductivity (DKSAT; Fig. 5d; Scott & van Wyk,
478 1990; Cerdà, 1998; Robichaud, 2000; Martin & Moody, 2001) from default values (Table B3).
479 Consistent with the hydrophobicity of burned soils, we calibrate the burn scar simulation by
480 systematically exploring a range of burn scar area saturated hydraulic conductivities (0 to 3×10^{-7}
481 m s^{-1} with a $5 \times 10^{-8} \text{ m s}^{-1}$ increment), with the goal of reproducing streamflow behavior similar to
482 USGS gage observations. We found that a value of $1.5 \times 10^{-7} \text{ m s}^{-1}$ gives the highest Nash-Sutcliffe
483 efficiency (NSE; Nash & Sutcliffe, 1970) across all three USGS stream gages (Table 1). NSE and
484 KGE are the two most widely used metrics for calibration and evaluation of hydrologic models.

485 The NSE has previously been used in streamflow calibration applications (e.g., Xia et al., 2012;
486 Bitew & Gebremichael, 2011), and it is calculated as follows:

487

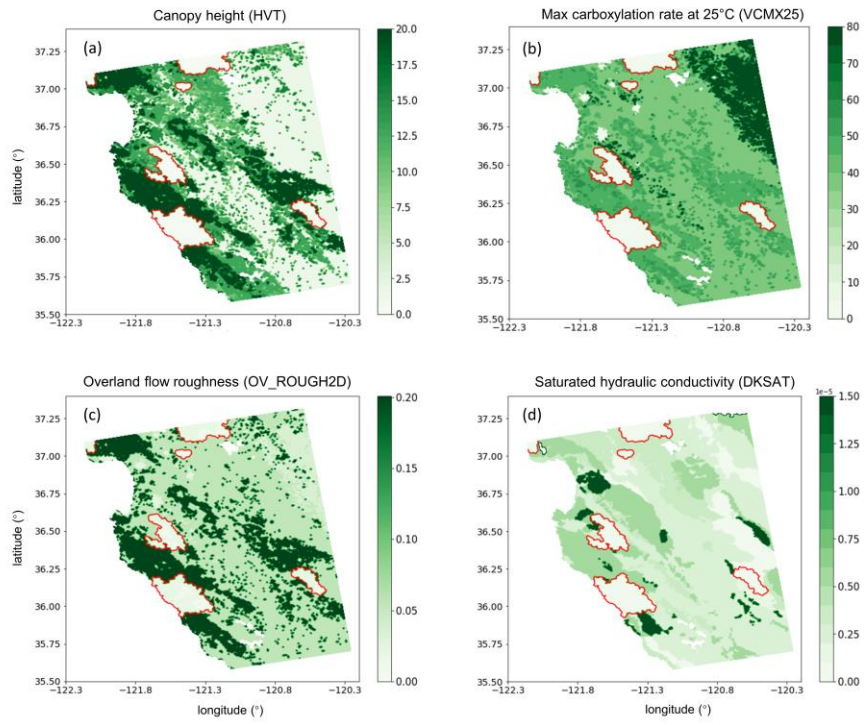
$$488 \quad NSE = 1 - \frac{\sum_{t=1}^{t=T} (Q_{sim}(t) - \overline{Q_{obs}(t)})^2}{\sum_{t=1}^{t=T} (Q_{obs}(t) - \overline{Q_{obs}})^2} \quad (14)$$

489

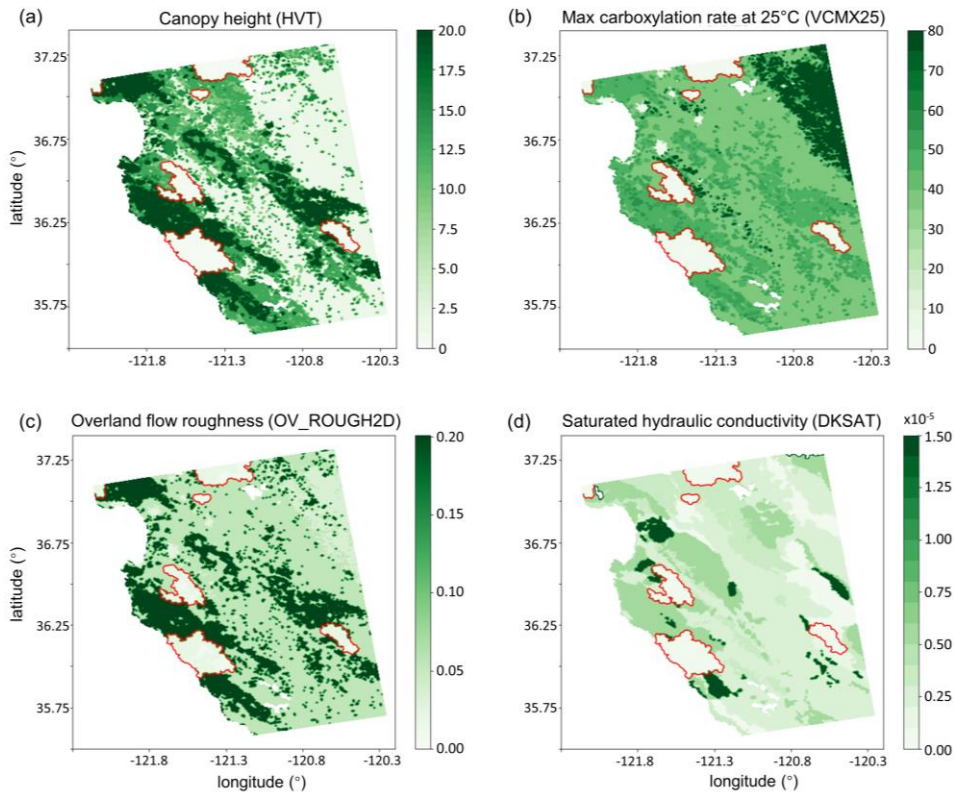
490 where T is the length of the time series, $Q_{sim}(t)$ and $Q_{obs}(t)$ are the simulated and observed
491 discharge at time t , respectively, and $\overline{Q_{obs}}$ is the mean observed discharge. By definition, NSEs of
492 1 indicate perfect correspondence between the simulated and observed streamflow. Positive NSEs
493 indicate that the model streamflow has a greater explanatory power than the mean of the
494 observations, whereas negative NSEs represent poor model performance (Moriasi et al., 2007;
495 Schaeffli & Gupta, 2007). When burn scar characteristics are included, evaluation metrics including
496 r , RMSE, and MAE all improve, while NSEs increase from negative values in the baseline to 0.84,
497 0.73, and 0.53 at gages 1870, 2000, and 2050, respectively. Higher correlation and NSE scores
498 and lower errors indicate the above mentioned burn scar parameter changes improve the model's
499 ability to simulate streamflow observations downstream of the burn scar (Table 1).

500

Parameter changes accounting for burn scar characteristics

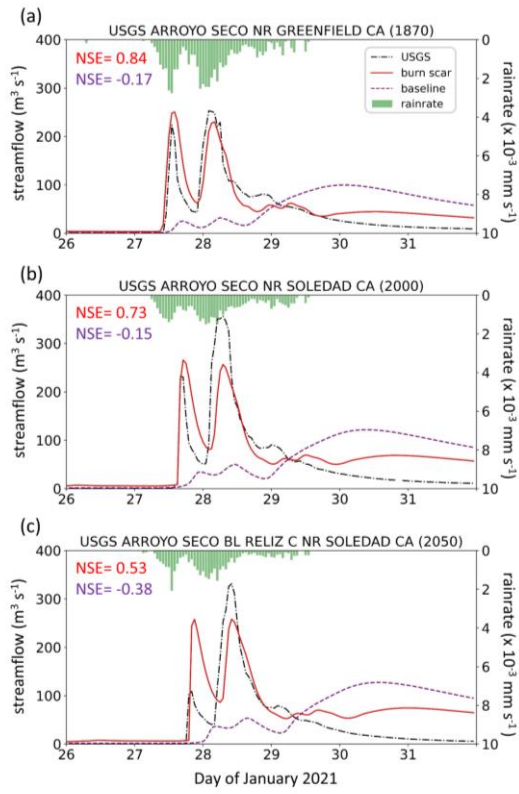


Parameter changes accounting for burn scar characteristics

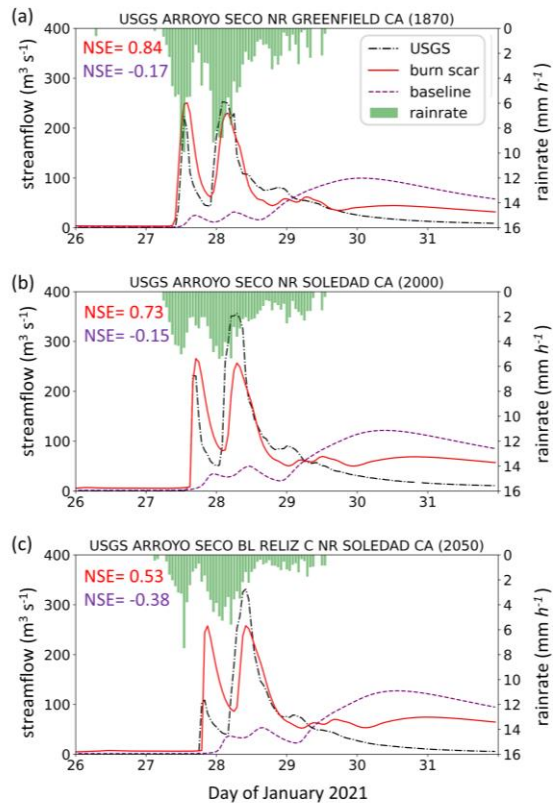


502
503 **Fig. 5]** Parameter setting in the WRF-Hydro burn scar simulation. (a) The height of the canopy
504 (HVT; m; shading), (b) maximum rate of carboxylation at 25°C (VCMX25; $\mu\text{mol CO}_2/(\text{m}^2 \cdot \text{s})$;
505 shading), (c) overland flow roughness coefficient (OV_ROUGH2D; shading), and (d) saturated
506 hydraulic conductivity (DKSAT; m s^{-1} ; shading) in the burn scar simulation.

MRMS precipitation, observed and simulated streamflow



MRMS precipitation, observed and simulated streamflow



508
 509 **Fig. 6** Precipitation, observed and simulated streamflow at three USGS stream gages. January 26–
 510 31, 2021 MRMS precipitation (mm h^{-1} ; green bars), observed ($\text{m}^3 \text{s}^{-1}$; black dash dotted line) and
 511 simulated streamflow in baseline simulation ($\text{m}^3 \text{s}^{-1}$; purple dashed line) and burn scar simulation
 512 ($\text{m}^3 \text{s}^{-1}$; red line) at (a) Arroyo Seco NR Greenfield, CA (ID 11151870), (b) Arroyo Seco NR
 513 Soledad, CA (ID 11152000), and (c) Arroyo Seco BL Reliz C NR Soledad, CA (ID 11152050).
 514 NSE scores for baseline (purple) and burn scar simulations (red) are shown at top left.
 515

516 **5 Results**

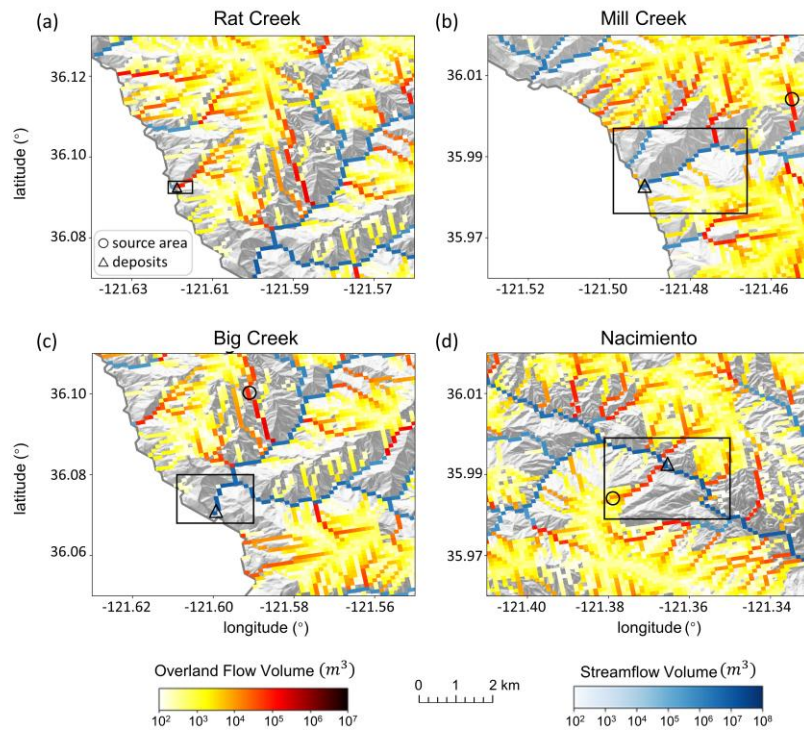
517 **5.1 Hydrologic response due to burn scar incorporation**

518 The pre-fire baseline simulation fails to capture the hydrologic behavior observed at the USGS
519 gages located within the burn scar (Fig. 6). Incorporation of burn scar characteristics substantially
520 alters the hydrologic response of the model and provides much higher fidelity streamflow
521 simulations (Fig. 6). Observed hydrographs are characterized by two early streamflow peaks
522 related to two precipitation bursts on January 27th and 28th. Our burn scar simulation captures this
523 behavior, while the baseline simulation streamflow peaks just once, with a lower magnitude and
524 an ~3-day lag after peak precipitation (Fig. 6). The steep rising limbs and high magnitude discharge
525 peaks of the burn scar hydrograph are indicative of flash flooding. Compared with the pre-fire
526 baseline scenario, the burn scar's barren land and low infiltration rate substantially accelerate
527 drainage rates and increase discharge volume into stream channels.
528

529 **5.2 Hydrologic response at four debris flow sites**

530 Mill Creek, Big Creek, and Nacimiento deposits are located in channels of 2nd Strahler stream
531 order or above so they are simulated as channelized streamflow in our WRF-Hydro simulations.
532 Due to its low stream order (1st Strahler stream order), Rat Creek is modeled entirely as overland
533 flow in our WRF-Hydro simulations. At the four debris flow sites, we use three metrics to
534 characterize hydrologic anomalies: (1) accumulated runoff volume, (2) peak discharge, and (3)
535 time to peak discharge. Fig. 7 depicts accumulated channelized discharge volume (blue shading)
536 and accumulated overland discharge volume (yellow-red shading) from January 27th 00:00 to 28th
537 12:00 near the four debris flow sites in the burn scar simulation. Accumulation time period is
538 chosen such that it covers the first two runoff surges in the simulated hydrographs which are likely
539 associated with debris flows (Fig. 8) given that nearly concurrent peak rainfall intensity and peak
540 discharge is a signature characteristic of debris flows (Kean et al., 2011). Runoff volume is on the
541 order of 10^4 m^3 at Rat Creek and 10^6 m^3 at the other three sites.

Simulated overland flow and streamflow in burn scar simulation

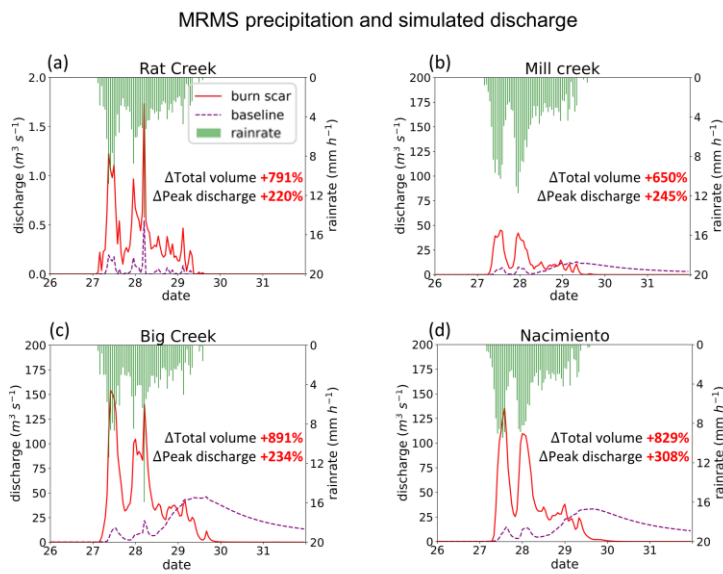


542
543 **Fig. 7|** WRF-Hydro simulated overland flow and streamflow in the burn scar simulation. (a)–(d)
544 Total volume of accumulated overland flow (m^3 ; yellow-red shading) and streamflow (m^3 ; blue
545 shading) between January 27th 00:00 and 28th 12:00 at four debris flow sites draped over a hillshade
546 of topography. Black rectangles correspond to domains in Fig. 3a–d. Black circles and triangles
547 indicate debris flow source areas and deposits, respectively.

548
549
550 Dramatic hydrographic changes after inclusion of burn scar characteristics are simulated at debris
551 flow source areas (Fig. B6 and Table B4) and deposition sites (Fig. 8 and Table 2). ~~WRF-Hydro~~
552 ~~facilitates investigation of the hydrologic response at triggering and deposit locations and along~~
553 ~~the runoff path.~~ Here, to emphasize the high susceptibility downstream, our analysis is focused on
554 debris flow deposits. At Rat Creek, where a section of CA1 collapsed, the magnitude of discharge
555 substantially increases, and overland flow surges are concurrent with rainfall bursts (Fig. 8a). Total

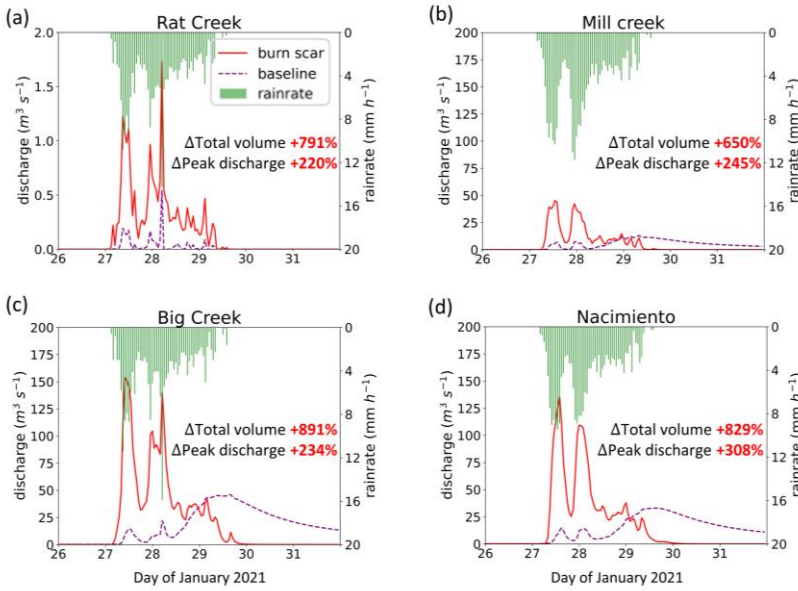
556 discharge accumulated during the AR event increases approximately eight-fold (791%), and peak
 557 discharge more than triples compared to the baseline simulation (Fig. 8a and Table 2). At Mill
 558 Creek, Big Creek, and Nacimiento, baseline hydrographs are characterized by less variability,
 559 muted responses to two early precipitation bursts, and a delayed third discharge peak that does not
 560 occur until ~3 days after AR passage (Fig. 8b–d). Maximum discharge peaks in the baseline
 561 hydrographs lag those in the burn scar simulation by ~2 days (Fig. 8b–d; Table 2). In the burn scar
 562 simulation, total volume substantially increases at the three channelized sites – total volume
 563 increases ~650% at Mill Creek, ~891% at Big Creek, and ~829% at Nacimiento (Fig. 8b–d and
 564 Table 2), and the absolute increase in volume is on the order of 10^6 m^3 (Table 2). Peak discharge
 565 more than triples at Mill Creek and Big Creek and more than quadruples at Nacimiento.
 566 Additionally, response times of the peak in discharge to the peak in precipitation decrease to less
 567 than an hour, highlighting the simulated flashiness of the burned catchments.

568



569

MRMS precipitation and simulated discharge



570
571
572 **Fig. 8** WRF-Hydro simulated discharge time-series at four debris flow deposition locations. (a)–
573 (d) MRMS precipitation (mm h^{-1} ; green bars) and simulated discharge time-series for January 26th
574 00:00 to 31st 23:00 at (a) Rat Creek, (b) Mill Creek, (c) Big Creek, and (d) Nacimiento deposition
575 locations (black triangles in Fig. 7a–d) in baseline simulation ($\text{m}^3 \text{s}^{-1}$; purple dashed line) and burn
576 scar simulation ($\text{m}^3 \text{s}^{-1}$; red line).

577

578

579 *Table 2*

580 *The total runoff volume, peak discharge, and peak timing at debris-flow deposits*

Site name	Baseline simulation			Burn scar simulation			
	Total volume (m^3)	Peak discharge ($\text{m}^3 \text{s}^{-1}$)	Highest peak timing	Total volume (m^3)	Peak discharge ($\text{m}^3 \text{s}^{-1}$)	1 st Peak timing	2 nd Peak timing
Rat Creek	6,897	0.54	28 th 05:00	61,425 (+791%)	1.73 (+220%)	27 th 09:00	28 th 05:00
Mill Creek	312,925	13.10	29 th 08:00	2,347,457	45.21	27 th 13:00	27 th 23:00

				(+650%)	(+245%)		
Big Creek	842,808	46.10	29 th 16:00	8,354,095 (+891%)	154.10 (+234%)	27 th 10:00	28 th 05:00
Nacimiento	743,531	33.15	29 th 16:00	6,904,706 (+829%)	135.41 (+308%)	27 th 14:00	28 th 00:00

581
582 **Table 2** | The total runoff volume, peak discharge, and peak timing in the baseline and burn scar
583 simulations from January 27th 00:00 to 31st 23:00 at deposition sites of Rat Creek, Mill Creek, Big
584 Creek, and Nacimiento debris flows (black triangles in Fig. 7a–d). The peak timing shown in the
585 baseline simulation is for the highest peak. The percent change of the total volume and peak
586 discharge in the burn scar simulation relative to the baseline simulation are shown in parentheses.
587
588

589 **5.3 Debris flow susceptibility assessment for the Dolan burn scar**

590 Since high magnitude runoff is often the cause and precursor of runoff-generated debris flows in
591 burned areas (Cannon et al., 2003, 2008; Rengers et al., 2016), we use ~~simulated accumulated~~
592 ~~volume~~~~peak discharge~~ of overland flow and streamflow to assess runoff-generated debris flow
593 susceptibility under pre-fire (i.e., baseline; Fig. 9a&d) and postfire (i.e., burn scar simulation; Fig.
594 9b&e) conditions. ~~we conduct similar analyses using accumulated discharge volume in Figs. B7–~~
595 ~~9 and Table B5 in Appendix B1.~~ We assess changes at both stream and catchment levels and use
596 the difference between burn scar and baseline simulations to assess added debris flow
597 susceptibility (Fig. 9c&f). Consistent with the increasing erosive and entrainment power associated
598 with increasing discharge, our debris flow susceptibility increases as ~~the accumulated peak~~
599 ~~discharge volume~~ increases. To reduce the effects of catchment size on the ~~volume peak discharge-~~
600 based susceptibility levels, we normalize a catchment’s discharge ~~volume~~ by the area of the
601 catchment (~~Santi & Morandi, 2013; Fig. Leopold et al., 1964; McCormick et al., 2009; Fig. 9d–f~~).
602 Non-normalized catchment susceptibility maps are also provided (Fig. ~~B7B10~~).

603
604 In the pre-fire baseline simulation, the AR-induced precipitation produces lower debris flow
605 susceptibility over most of the domain, but elevated susceptibility along stream channels (Fig. 9a).
606 We note no substantial differences between areas in or out of the burn scar. In the burn scar
607 simulation, debris flow susceptibility levels increase across the Dolan burn scar and along channels
608 outside but downstream of the burn scar (Fig. 9b–c). The ~~peak discharge volume increases by an~~
609 ~~order of magnitude~~ near Rat Creek, Big Creek, Mill Creek, and Nacimiento. ~~more than triples~~
610 (Table 2 & Fig. 9a–c). Within the burn scar, susceptibility along major stream channels, such as
611 the Nacimiento River and San Antonio River increase. Outside the burn scar, susceptibility levels
612 along river channels downstream of the burn scar, such as the Arroyo Seco River, also increase
613 (Fig. 9c).

614
 615 At the catchment level, debris flow susceptibility is assessed using ~~accumulated peak~~ discharge
 616 ~~volumes~~ normalized by catchment areas (Fig. 9d-f). ~~Accumulated discharge volumes are~~
 617 ~~calculated~~ at the outlet of each catchment between January 27th 00:00 to 28th 12:00 (Fig. 9d-f).
 618 The catchment-area normalized ~~volume is then used as the susceptibility index and peak discharge~~
 619 is classified into five categories based on equal intervals on log₁₀ scale. The susceptibility
 620 categorization follows: “very low” (~~~10³10⁻² m³ s⁻¹ km⁻²~~), “low” (~~~10⁴10⁻¹ m³ s⁻¹ km⁻²~~), “medium”
 621 (~~~10⁵10⁰ m³ s⁻¹ km⁻²~~), “high” (~~~10⁶10¹ m³ s⁻¹ km⁻²~~), and “very high” (~~~10⁷10² m³ s⁻¹ km⁻²~~). In the
 622 baseline simulation, majority of catchments are subject to low or very low debris flow
 623 susceptibility with ~~total~~ normalized ~~peak discharge volume~~ less than ~~10⁴1 m³ s⁻¹ km⁻²~~ (Fig. 9d). In
 624 the burn scar simulation, about half of the catchments within the Dolan burn scar have medium
 625 susceptibility or above, and about 1/4 of basins are subject to high ~~to very high~~ debris flow
 626 susceptibility (Fig. 9e and Table 3). The additional debris flow susceptibility brought about by the
 627 inclusion of wildfire burn scar characteristics is substantial (Fig. 9f).
 628

629 To summarize changes in debris flow susceptibility as a result of including burn scar
 630 characteristics in WRF-Hydro simulations, we create distributions of pre-fire baseline and burn
 631 scar catchment-area normalized ~~peak~~ discharge from the 404 catchments located within the Dolan
 632 burn scar perimeter (Fig. 10). After incorporating burn scar characteristics, the full distribution
 633 shifts to the right, indicating increased susceptibility levels – a shift considered robust by a
 634 Student’s t-test (p value: ~~4.6E-455.3E-23~~). A quantitative assessment of this shift indicates that
 635 ~~both the mean and the standard deviation of~~ catchment area normalized ~~peak discharge volume~~
 636 ~~increases/increase~~ by ~~~1300%~~ while the standard deviation ~~increases~~ ~~~1400%~~ ~~more than 300%~~ (Table
 637 3). We also assess shifts at a range of distribution percentiles: 5P: ~~148375%~~, 25P: ~~725500%~~, 50P:
 638 ~~924447%~~, 75P: ~~980341%~~, and 95P: ~~1300366%~~ (Table 3). In the burn scar simulation, ~~nearly more~~
 639 ~~than~~ half of catchments have normalized ~~volumes > 10⁵ m³ peak discharge > 10⁰ m³ s⁻¹ km⁻²~~ (i.e.,
 640 medium susceptibility) and about 1/4 of catchments have ~~volumes > 10⁶ m³ normalized peak~~
 641 ~~discharge > 10¹ m³ s⁻¹ km⁻²~~ (i.e., high susceptibility) – values that correspond to the ~~75P70P~~ and
 642 90P of the baseline simulation, respectively. Disproportionate shifting of the ~~right tail of the~~
 643 distribution suggests that ~~extreme~~ debris flow susceptibility increases non-linearly under simulated
 644 burn scar conditions.

Formatted: Font color: Auto, Superscript
 Formatted: Font color: Auto, Superscript
 Formatted: Font color: Auto

645 ~~Table 3~~
 646 ~~Statistics of catchment area normalized discharge volume in baseline and burn scar simulations~~

	mean	std	5P	25P	50P	75P	95P
Baseline simulation (m ³ ·km ⁻²)	380k	±1.6M	0.6k	3.7k	13k	120k	2.1M
Burn-scar	5.5M	±23.0M	1.5k	30.7k	135k	1.3M	29.1M

simulation (m³·km⁻²)							
Relative percent change	1300%	1400%	148%	725%	924%	980%	1300%

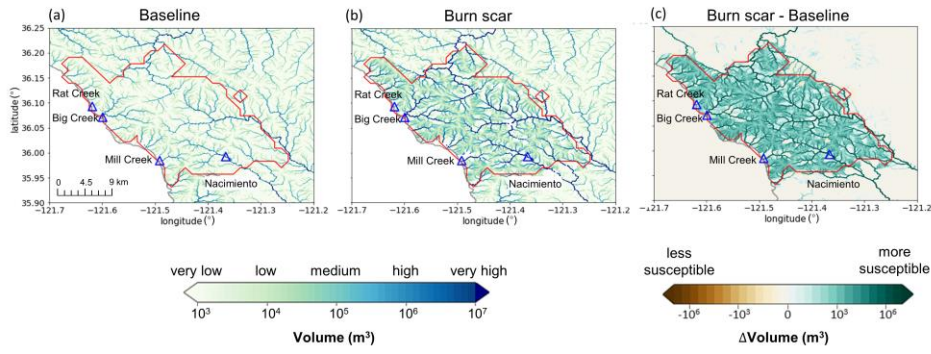
647 **Table 3** | ~~Statistics, including the mean, standard deviation (std), 5P, 25P, 50P, 75P, and 95P, of~~
648 ~~the catchment area normalized discharge volume for all basins within the Dolan burn scar in the~~
649 ~~baseline and burn scar simulation and their relative percent changes.~~

650

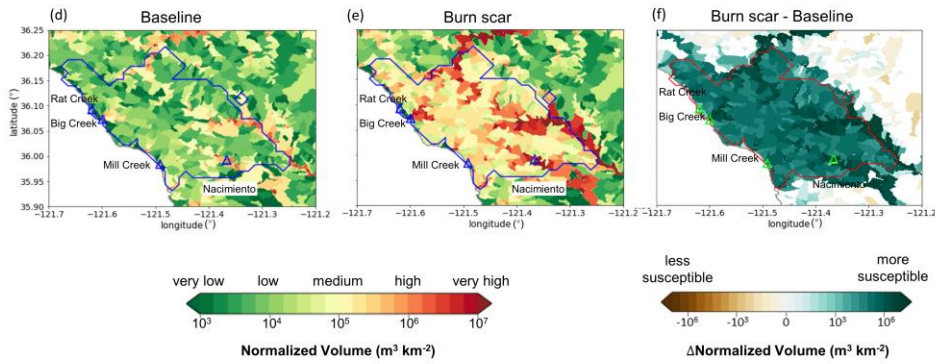
651 Our catchment-area normalized ~~peak discharge volume~~-based susceptibility assessment also
652 indicates that the catchments containing Mill Creek, Big Creek, and Nacimiento have high or very
653 high susceptibility (Fig. 9d–f), consistent with our (limited) debris flow observations. Other areas
654 with elevated susceptibility include catchments containing the Arroyo Seco and San Antonio
655 Rivers. Beyond the burn scar perimeter, effects of fire expand to adjacent and downstream
656 catchments, and some drainage basins along the Arroyo Seco and Nacimiento Rivers are simulated
657 to have very high susceptibility, i.e., normalized ~~peak discharge volumes in excess of 10⁷ exceeds~~
658 ~~10² m³ s⁻¹ km⁻²~~ (Fig. 9e&f).

659

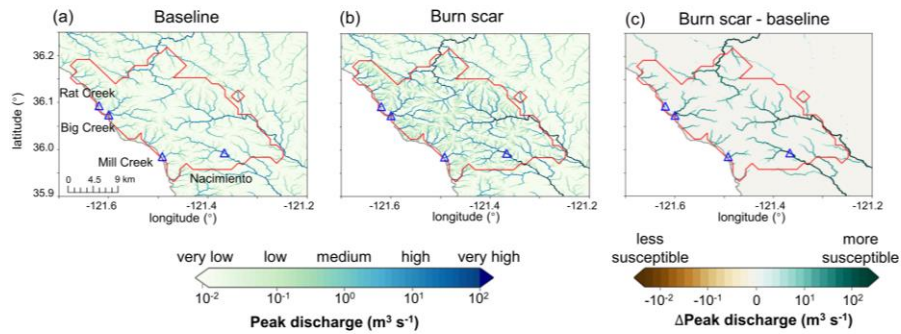
Postfire Debris Flow Susceptibility



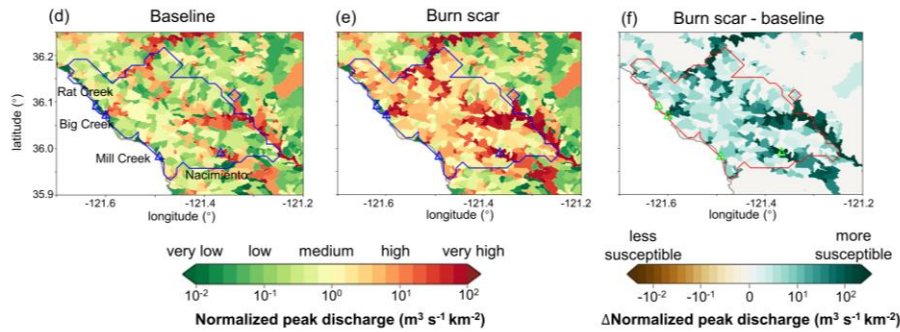
Catchment-area Normalized Postfire Debris Flow Susceptibility



Postfire debris flow susceptibility



Catchment-area normalized postfire debris flow susceptibility



661

662

663

664

665

666

667

668

669

670

671

672

673

674

675

Fig. 9 | ~~Discharge volume~~Peak discharge-based postfire debris flow susceptibility. ~~Debris flow susceptibility~~Peak discharge at individual stream level for the (a) baseline, (b) burn scar, and (c) difference between burn scar and baseline simulations. ~~Susceptibility is estimated as total discharge volume~~ from January 27th 00:00 to 28th 12:00: ~~($m^3 s^{-1}$)~~. (d)–(f) Normalized ~~debris flow susceptibility~~peak discharge by catchment area at catchment level: ~~($m^3 s^{-1} km^{-2}$; shading)~~. For each catchment, the ~~susceptibility is determined by total~~peak discharge ~~volume is the maximum discharge rate~~ at the catchment outlet from January 27th 00:00 to 28th 12:00 divided by catchment area. Triangles stand for debris flow deposition locations and are annotated in (a) and (d). We conduct similar analyses using accumulated discharge volume in Fig. B7 in Appendix B.

Formatted: Font: Not Bold, Font color: Auto

Formatted: Right

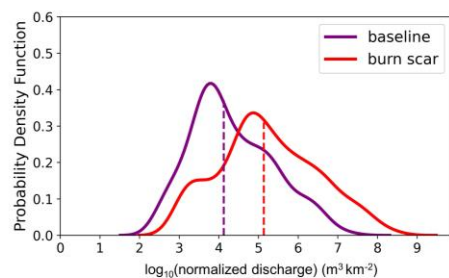
Formatted: Right: 0.33"

Formatted: Superscript

Formatted: Superscript

Formatted: Font color: Auto

676

677 Table 3

678

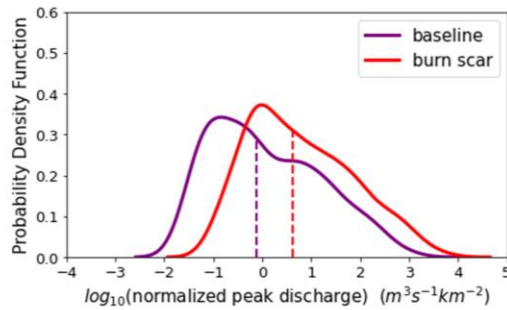
679 Statistics of catchment area-normalized peak discharge in baseline and burn scar simulations

	<u>mean</u>	<u>std</u>	<u>5P</u>	<u>25P</u>	<u>50P</u>	<u>75P</u>	<u>95P</u>
<u>Baseline simulation</u> ($\text{m}^3 \text{s}^{-1} \text{km}^{-2}$)	<u>25.88</u>	<u>± 95.71</u>	<u>0.04</u>	<u>0.14</u>	<u>0.76</u>	<u>8.21</u>	<u>129.54</u>
<u>Burn scar simulation</u> ($\text{m}^3 \text{s}^{-1} \text{km}^{-2}$)	<u>110.80</u>	<u>± 423.82</u>	<u>0.19</u>	<u>0.84</u>	<u>4.16</u>	<u>36.21</u>	<u>603.15</u>
<u>Relative percent change</u>	<u>328%</u>	<u>343%</u>	<u>375%</u>	<u>500%</u>	<u>447%</u>	<u>341%</u>	<u>366%</u>

680 Table 3| Statistics, including the mean, standard deviation (std), 5P, 25P, 50P, 75P, and 95P, of
 681 the catchment-area normalized peak discharge for all the 404 basins within the Dolan burn scar in
 682 the baseline and burn scar simulation and their relative percent changes. We conduct similar
 683 analyses using accumulated discharge volume in Table B5 in Appendix B.

684

Distribution of catchment-area normalized peak discharge



685

686 **Fig. 10** Distributions of ~~accumulated peak discharge volumes~~ at the outlet of the 404 catchments
687 normalized by upstream catchment areas within Dolan burn scar in the baseline simulation (purple
688 line) and in the burn scar simulation (red line). Dashed vertical lines indicate median values. ~~We~~
689 conduct similar analyses using accumulated discharge volume in Fig. B8 in Appendix B.

690

691 **6 Discussion**

692 Given the historic and growing frequency of wildfires in the western U.S. (Williams et al., 2019;
693 Goss et al., 2020; Swain 2021) and globally (Flannigan et al., 2013; Jolly et al., 2015), developing
694 tools to investigate, better understand, and potentially predict changes in burn scar hydrology and
695 natural hazards at regional scales is critical. Here, we demonstrate the first use of WRF-Hydro to
696 simulate the susceptibility of a burn scar to postfire debris flows during a landfalling AR. We
697 augmented the default version of WRF-Hydro to output overland flow and to replicate burn scar
698 behavior by adjusting vegetation type and infiltration rate parameters. WRF-Hydro simulations
699 were validated against PSL soil moisture and USGS streamflow observations before we used
700 simulated peak discharge of streamflow and overland flow volumes to characterize debris flow
701 susceptibility. A comparison between baseline and burn scar simulations demonstrated that
702 changes in hydraulic properties of burned areas causes drastic changes in surface flows, including
703 faster discharge response times, and greater peak discharge and total volumes, consistent with
704 findings from previous postfire hydrology studies (Anderson et al., 1976; Scott, 1993; Meixner &
705 Wohlgemuth, 2003; Kean et al., 2011; Kinoshita & Hogue, 2015; Brunkal & Santi, 2016; Williams
706 et al., 2022). At the catchment level, for the 404 catchments located within the Dolan burn scar,
707 median catchment area-normalized volume peak discharge increases nine-fold by ~450% relative

708 to the baseline. In addition, Mill Creek, Big Creek, and Nacimiento basins were simulated to have
709 high-to-very high debris flow susceptibility, corresponding well with identified debris flow
710 occurrences.

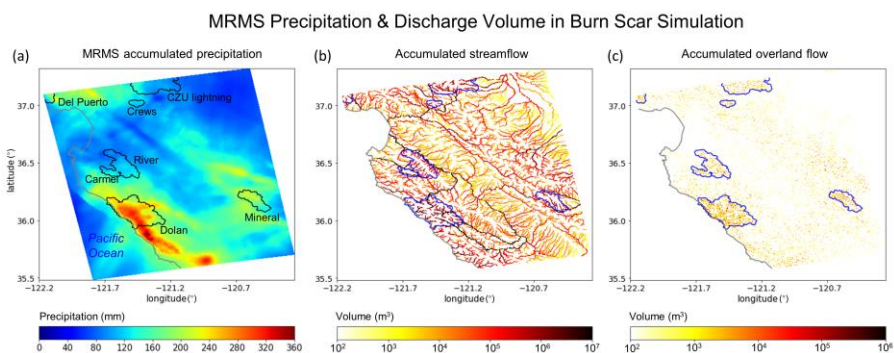
711
712 Despite methodological differences, our debris flow susceptibility map for this AR event is
713 generally consistent with the USGS' postfire, pre-AR, design-storm-based preliminary hazard
714 assessment (USGS, 2020). As described above, USGS preliminary hazard assessments use logistic
715 regression models to estimate the likelihood of debris flow occurrence and multivariate linear
716 regression models to estimate debris flow volumes. The USGS empirical approach is trained on
717 historical western U.S. debris flow occurrence and magnitude data and incorporates burn scar soil
718 erodibility and burn severity data (Cannon et al., 2010; Gartner et al., 2014; Staley et al., 2016).
719 For precipitation, the USGS assessment utilizes a design storm approach that assumes 1–5 year
720 return interval magnitude precipitation falls uniformly over a region/burn scar (USGS, 2020). For
721 the Dolan burn scar, both assessments find that large stream channels had relatively higher
722 susceptibility than small streams or overland areas. However, a close comparison of the two maps
723 reveals differences in spatial distribution of hazardous catchments. In the USGS assessment,
724 higher likelihood is predicted north and southeast of the burn scar, whereas in our assessment the
725 highest susceptibility occurs along major stream channels. We hypothesize that USGS-assessed
726 areas of higher hazard potential are related to their use of spatially uniform design-storm
727 precipitation (see Fig. 2 for MRMS precipitation footprint) and burn severity data (Burned Area
728 Emergency Response, 2020).

729
730 Comparison with the USGS hazard assessment framework suggests room for improvement in
731 WRF-Hydro-based assessments (i.e., inclusion of burn severity and soil erodibility data), but also
732 highlights the potential utility of working with spatially-distributed and time-varying precipitation.
733 However, this also means the accuracy of WRF-Hydro predictions depends on the accuracy of
734 precipitation forcing, and in our hindcast application, MRMS precipitation data (Appendix A).
735 Accordingly, our WRF-Hydro-based assessment could benefit from precipitation products
736 mosaiced from various sources to constrain precipitation-based uncertainties (e.g., gauge-
737 corrected and/or Mountain Mapper MRMS), although the long processing time of these datasets
738 inhibits timely post-event assessments.

739 In addition to the above results focused primarily on the Dolan burn scar, a key feature of WRF-
740 Hydro is its ability to simulate the land surface hydrology of expansive geographic domains, e.g.,
741 NOAA runs the National Water Model over the entire continental U.S. Development of tools
742 capable of regional susceptibility assessments is crucial, particularly in a wildfire-prone region
743 like California, due to the large spatial scale, diverse morphology, and often tight spatial gradients
744 of precipitation events and their interactions with geographically widespread wildfire burn scars.
745 For example, landfalling ARs are often long (1000s of km) filament-like systems with
746 heterogeneous intensity gradients along their length. As a demonstration of wide geographic
747 applicability, we assess susceptibility over our full model domain which includes more than 10,000

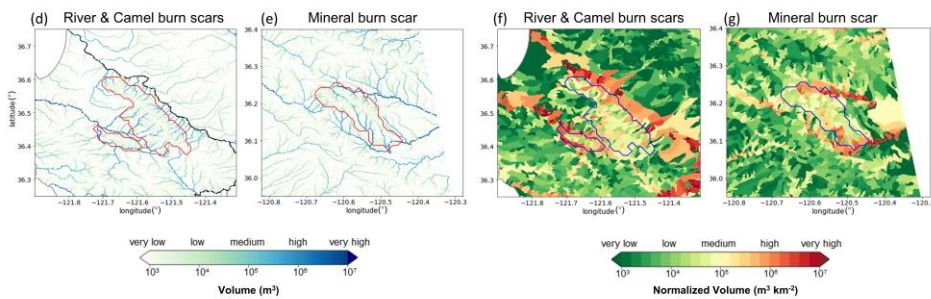
748 catchments and a number of 2020 wildfire burn scars in addition to the Dolan burn scar (Fig 11).
749 The domain-wide analysis reveals elevated peak discharge ~~volume~~, i.e., elevated susceptibility, in
750 areas of high precipitation and in burned terrains (Figs. 11a–c). We highlight channelized and
751 catchment-area normalized debris flow susceptibility in non-Dolan burn scar sites in Figs. 11d–g.
752 In an operational forecast context, the ability to simulate landslide and debris flow susceptibilities
753 and hazards over numerous catchments at meteorologically appropriate scales represents a step-
754 change in the field. We argue that our demonstration of WRF-Hydro’s debris flow susceptibility

755 hindcast capabilities should motivate further exploration and development for potential use in
 756 operational hazard forecasting.



Postfire Debris Flow Susceptibility

Catchment-area Normalized Postfire Debris Flow Susceptibility

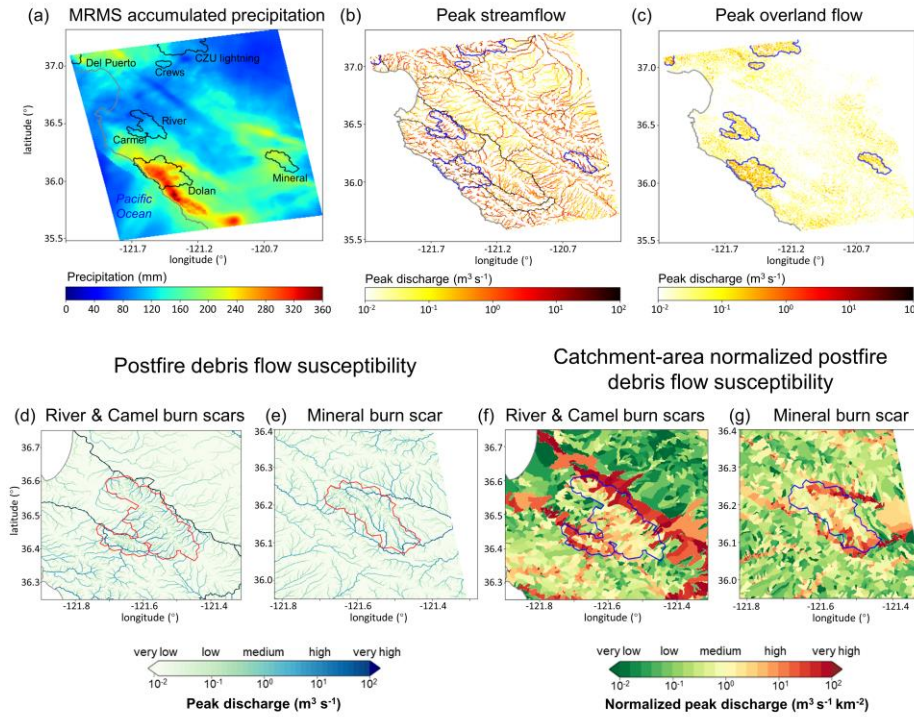


757

758

759

MRMS precipitation & peak discharge in burn scar simulation



760
 761 **Fig. 11** MRMS accumulated precipitation and **peak discharge** informed regional debris flow susceptibility. (a) MRMS accumulated precipitation during January 27th 00:00 to 29th 23:00
 762 over the model domain (**mm**; shading: **mm**). Names of burn scars are labeled in black. (b)
 763 **Accumulated Peak** streamflow (**m³ s⁻¹**; yellow-to-red shading: **m³**) and (c) **accumulated peak**
 764 **overland flow** from 27th 00:00 to 28th 12:00 over the model domain (**m³ s⁻¹**; yellow-to-red shading:
 765 **m³**). (d)–(e) Stream-level postfire debris flow susceptibility as Fig. 9b but for River and Camel
 766 burn scars. (f)–(g) Catchment-area normalized debris flow susceptibility as Fig. 9e but for River
 767 and Camel burn scars. Wildfire perimeters of 2020 wildfire season are outlined in black in (a), in
 768 blue in (b), (c), (f), and (g), and in red in (d) and (e). The coastline of California is depicted in grey.

770
 771 In addition to investigating the operationalization of WRF-Hydro’s natural hazard prediction
 772 capabilities, we note that **with additional work** our susceptibility-focused methodology could be
 773 advanced to **the level of** hazard assessment, in line with current USGS **debris flow** products. The
 774 USGS Emergency Assessment of Postfire Debris-flow Hazard predicts debris flow volume and

775 likelihood. To advance from susceptibility to hazard assessment, our methodology would need to
776 incorporate both debris flow volume estimates and occurrence likelihoods. In the following, we
777 highlight research directions that could help advance our susceptibility-focused methodological
778 framework. ~~WRF-Hydro is a water-only model. While water-only models have been widely used
779 to investigate and better understand debris flow dynamics (Arattano & Savage, 1994; Tognacca et
780 al., 2000; Arattano & Franzi, 2010; Rengers et al., 2016; McGuire & Youberg, 2020; Di Cristo et
781 al., 2021), sediment supply, soil erodibility, and other sedimentological factors play important
782 roles in determining the potential for and severity of mass failure events (McGuire et al., 2017).~~
783 ~~Developing~~The first capability to develop would be a runoff-generated debris flow model that
784 couples hydrologic and sediment erosion and transport processes ~~could~~to help ~~to~~ characterize
785 postfire debris flow volumes. Indeed, previous efforts have demonstrated the capacity to couple
786 WRF-Hydro with sediment flux models (Yin et al., 2020; Shen et al., 2021). In addition to
787 sediments, burn scar ash can comprise a substantial fraction of the total debris flow volume (e.g.,
788 Reneau et al., 2007). As such, efforts to constrain ash availability and entrainment in hydrologic
789 flows could prove fortuitous in hazard assessment and prediction efforts. A second capability in
790 need of development is the use of WRF-Hydro to identify debris flow triggering time and location
791 by employing a domain-specific rainfall ID threshold trained with historic landslide inventory and
792 triggering rainfall events (Tognacca et al., 2000; Gregoretti & Dalla Fontana, 2007, 2008) or a
793 newly developed dimensionless discharge and Shields stress threshold (Tang et al., 2019a;
794 McGuire & Youberg, 2020). While in this study we do not attempt to simulate debris flow
795 dynamics such as triggering, we note that WRF-Hydro is capable of simulating overland flow and
796 streamflow at higher spatiotemporal resolutions [on scales that are similar to other debris flow
797 mechanistic studies such as Rengers et al. (2016), McGuire et al. (2016, 2017), and Tang et al.
798 (2019a, 2019b)]. Therefore, WRF-Hydro's capability to simulate the triggering processes of
799 runoff-generated debris flows is potentially only limited by the spatiotemporal resolution of
800 precipitation forcing and computing resources.

801
802 In addition to constraining ~~potential~~ postfire debris flow volumes and occurrence likelihoods,
803 WRF-Hydro's application in debris flow studies could be advanced via concerted engagement with
804 uncertainties that are both external (meteorological forcing data) and internal (physical parameters)
805 to the model. Previous studies have demonstrated that precipitation is often the largest source of
806 uncertainty in hydrologic predictive models (Hapuarachchi et al., 2011; Alfieri et al., 2012).
807 Engagement with precipitation forcing uncertainties in past, near-term, and future contexts could
808 provide probabilistic nuance to natural hazard investigations. For example, (a) debris flow hindcast
809 studies could use a diversity of precipitation datasets to isolate precipitation-derived debris flow
810 uncertainties in historic events, (b) operational forecast efforts could utilize ensemble-based
811 weather forecast data to inform likelihood statements in debris flow hazard assessments, and (c)
812 probabilistic projections of debris flow likelihood in future climates could assess and partition
813 uncertainties derived from emission pathway, model structure, or internal variability effects on
814 meteorological forcings (Nikolopoulos et al., 2019; Hawkins & Sutton, 2009; Deser et al., 2020).

815 Uncertainties internal to WRF-Hydro are also ripe for investigation. Probabilistic predictions
816 crafted from an ensemble of perturbed model physics simulations have been used to predict
817 rainfall-triggered shallow landslides (Raia et al., 2014; Canli et al., 2018; Zhang et al., 2018).
818 Similar efforts using WRF-Hydro could target post-wildfire debris flows.

819
820
821 Lastly, the above discussion of potential WRF-Hydro applications and advancements speaks to the
822 adaptability and customization of this open-source numerical model. An additional layer of WRF-
823 Hydro’s adaptability concerns its geographic focus. While we calibrate and use the model over a
824 central California domain, the choice of geographic footprint is only limited by the availability of
825 requisite initial and boundary conditions, environmental observations for calibration, and
826 computational resources. For use in non-central California domains, we recommend calibration
827 beginning with the default version of the model. Given the ecological and geological diversity of
828 locations that experience wildfires and debris flows, it is likely that calibrations distinct from those
829 reported here will be needed in different regions. For example, soil sealing effects, infiltration, and
830 runoff in wetter and more vegetated locations, such as Oregon, USA, behave differently than those
831 in central California (Palmer, 2022). As such, calibration of relevant model parameters (e.g.,
832 saturated hydraulic conductivities) should be based on a physics-informed approach that accounts
833 for local environmental conditions and hydrologic behaviors. Indeed, given the ability to simulate
834 large heterogeneous geographic domains, it is likely that different regions within a given domain
835 may require different calibration schemes. As WRF-Hydro is fully distributed, spatially
836 heterogeneous calibrations are non-problematic. This spatial adaptability may prove particularly
837 helpful in post-wildfire debris flow hazard assessments when considering multiple generations of
838 wildfires and variable degrees of burn scar severity and recovery.

839 **7 Conclusion**

840 Here we augment WRF-Hydro to assess regional postfire debris flow susceptibility. Our
841 methodology involves output of simulated overland flow data and alteration of the model’s
842 representation of burn scars. In this application we have balanced the computational cost of a
843 regional domain with our choice of resolved spatial resolution for terrain routing and overland
844 flow calculations (100 m). However, WRF-Hydro has previously been applied to smaller domains
845 at higher terrain routing resolutions (~30 m). Future work could assess the use of the model to
846 study burn scar hydrology at finer spatial scales, should the application warrant and should
847 underlying data at sufficient resolution exist. Other potential applications of our augmented model
848 framework include alpine areas and steep hillslopes with sparse vegetation where runoff-generated
849 debris flows dominate over landslide-initiated ones (Davies et al., 1992; Coe et al., 2003, 2008).
850 Furthermore, our burn scar parameter changes are performed to Noah-MP, which is the core land
851 surface component of the NCEP Global Forecast System (GFS) and Climate Forecast System
852 (CFS), thus the findings presented herein, are likely to prove useful in the broader worlds of
853 forecast meteorology and climate science. In addition, here WRF-Hydro is driven by historical

854 precipitation and meteorological data, i.e., in hindcast mode. However, this modeling framework
855 could also be employed to project hazards under future climatic conditions (e.g., Huang et al.,
856 ~~2020~~2020a), or given its relatively low computational expense, in operational forecast mode.
857 Indeed, modern ensemble-based meteorological forecasting could provide high spatiotemporal
858 forcing data with which disaster preparedness managers could probabilistically assess debris flow
859 hazard potential, and issue advanced life and property saving warnings.

860
861
862

863 Appendix A

864 Text A1. Multi-Radar/Multi-Sensor System (MRMS) radar-only precipitation estimate and 865 uncertainty

866 MRMS is a precipitation product that covers the contiguous United States (CONUS) on 1-km grids.
867 It combines precipitation estimates from sensors and observational networks (Zhang et al.,
868 2011, 2014, 2016), and is produced at the National Centers for Environmental Prediction (NCEP)
869 and distributed to National Weather Service forecast offices and other agencies. Input datasets
870 used to produce MRMS include the U.S. Weather Surveillance Radar-1988 Doppler (WSR-88D)
871 network and Canadian radar network, Parameter-elevation Regressions on Independent Slopes
872 Model (PRISM; Daly et al., 1994, 2017), Hydrometeorological Automated Data System (HADS)
873 gauge data with quality control (Qi et al., 2016), and outputs from numerical weather prediction
874 models. There are four different MRMS quantitative precipitation estimates (QPE) products
875 incorporating different input data or combinations: radar only, gauge only, gauge-adjusted radar,
876 and Mountain Mapper. One caveat of using MRMS is that weather radars are problematic in
877 accurately capturing rainfall in high mountainous areas due to beam blocking by the orography
878 (Anagnostou et al., 2010; Germann et al., 2007), and gauge-corrected and Mountain Mapper
879 MRMS are superior and preferred. However, for our study period (i.e., January 1–31, 2021), **only**
880 **the radar only QPE is** the gauge-corrected and Mountain Mapper MRMS are not available (as of
881 **November 2021** May 2022).

Formatted: Not Highlight

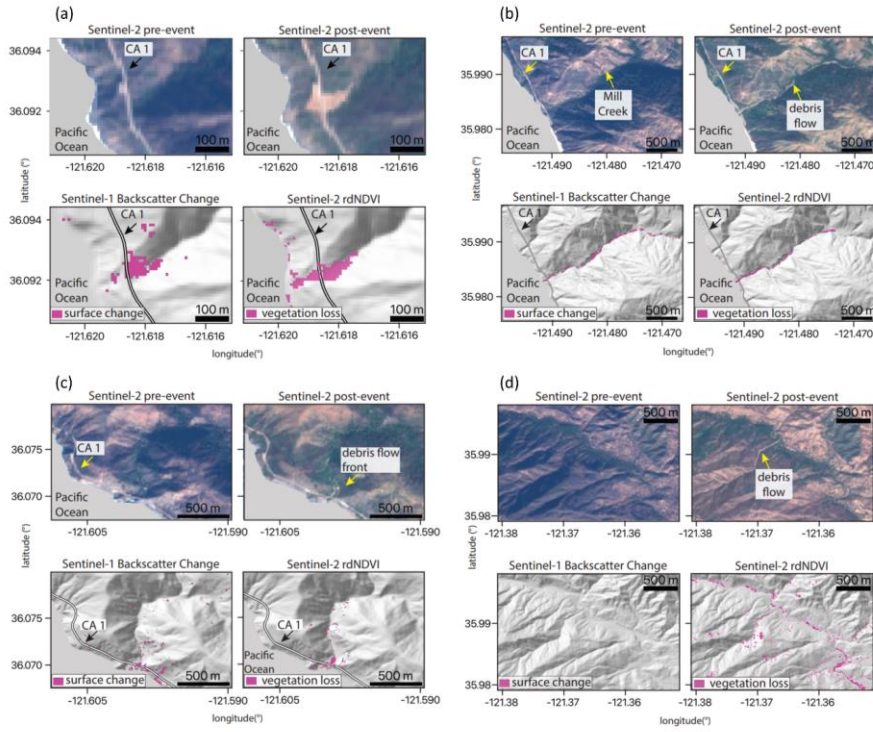
Formatted: Not Highlight

Formatted: Not Highlight

882

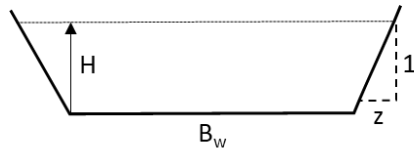
883 We acknowledge that precipitation data has uncertainties. Use of different precipitation products
884 may produce different results. A study comparing different gridded precipitation datasets including
885 satellite-based precipitation data, gauge dataset, and multi-sensor products revealed large
886 uncertainties in precipitation intensity (Bytheway et al., 2020). However, comparing different
887 precipitation datasets to characterize uncertainties is beyond the scope of this study. MRMS
888 provides gridded precipitation at high temporal (hourly) and spatial (1-km) resolutions, making it
889 a useful tool to demonstrate the utility of WRF-Hydro in post-wildfire debris flow susceptibility
890 assessments.

891 **Appendix B**



892
 893
 894 **Fig. B1** Optical- and SAR-based remote sensing data of four debris flows. Optical data from
 895 Sentinel-2 show pre- and post-debris flow imagery in real color. rdNDVI calculated from the
 896 Sentinel-2 data show a decrease in vegetation corresponding to debris flow locations. Sentinel-1
 897 backscatter change shows the change in ground surface properties determined by calculating the
 898 log ratio of pre- and post-event SAR images. The pre-event, post-event satellite images, Sentinel-
 899 1 Backscatter, and Sentinel-2 rdNDVI change at (a) Rat Creek, (b) Mill Creek, (c) Big Creek, and
 900 (d) Nacimiento.

901
 902
 903



904
905 **Fig. B2** Schematic trapezoidal shape and related parameters of channels in WRF-Hydro. B_w is
906 the channel bottom width (m), z is the channel side slope (m), and H is water elevation (m). The
907 cross-sectional area of flow is calculated as $(B_w + H z)H$.

908

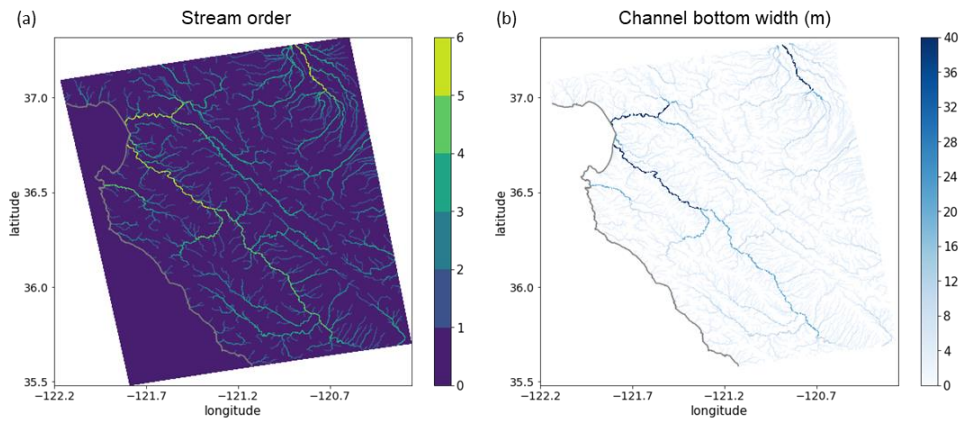
909 **Table B1 Parameters of trapezoidal channels in WRF-Hydro.**

Stream order	Channel bottom width B_w (m)	Channel side slope z (m)	Manning's roughness coefficient n
1	1.5	3	0.33
2	3	1	0.21
3	5	0.5	0.09
4	10	0.18	0.06
5	20	0.05	0.04
6	40	0.05	0.03
7	60	0.05	0.02
8	70	0.05	0.02
9	80	0.05	0.01
10	100	0.05	0.01

910
911 **Table B1** Parameters of the trapezoidal channels in WRF-Hydro including channel bottom width
912 B_w (m), channel side slope z (m), and Manning's roughness coefficient n .

913

914



915
 916 **Fig. B3** (a) Stream order defined by the USGS 30-m DEM in our WRF-Hydro model domain
 917 and (b) the channel bottom width (m) which is a function of stream order (Table B1).
 918

919 *Table B2*

920 *MODIS IGBP 20-category land cover type and properties in Noah-MP LSM*

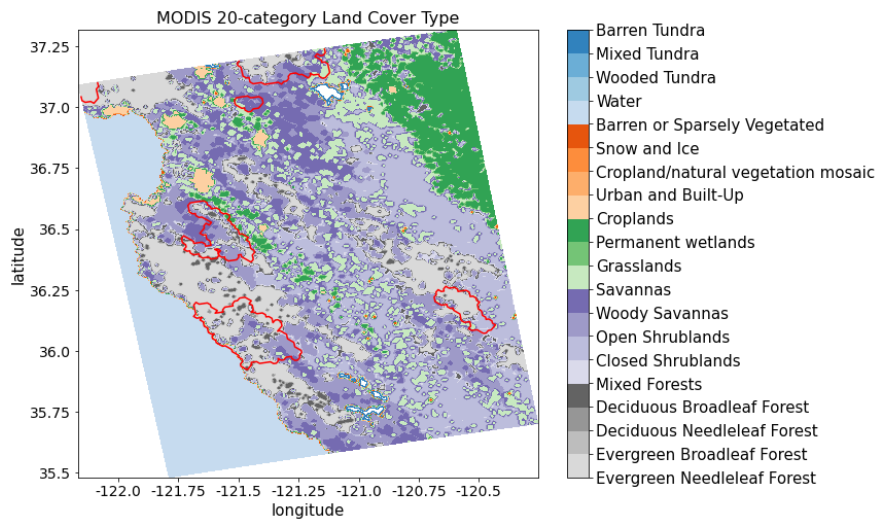
Land cover code	Land cover type	Canopy height (m)	Max carboxylation rate at 25°C ($\mu\text{mol CO}_2/(\text{m}^2 \cdot \text{s})$)	Overland flow roughness
1	Evergreen Needleleaf Forest	20	50	0.2
2	Evergreen Broadleaf Forest	20	60	0.2
3	Deciduous Needleleaf Forest	18	60	0.2
4	Deciduous Broadleaf Forest	16	60	0.2
5	Mixed Forests	16	55	0.2
6	Closed Shrublands	1.1	40	0.055
7	Open Shrublands	1.1	40	0.055
8	Woody Savannas	13	40	0.055
9	Savannas	10	40	0.055
10	Grasslands	1	40	0.055
11	Permanent wetlands	5	50	0.07
12	Croplands	2	80	0.035
13	Urban and Built-Up	15	0	0.025
14	Cropland/natural vegetation mosaic	1.5	60	0.035
15	Snow and Ice	0	0	0.01
16	Barren or Sparsely Vegetated	0	0	0.035
17	Water	0	0	0.005
18	Wooded Tundra	4	50	0.055
19	Mixed Tundra	2	50	0.055
20	Barren Tundra	0.5	50	0.055

921

922 **Table B2** MODIS IGBP 20-category land cover type and properties in Noah-MP LSM.

923

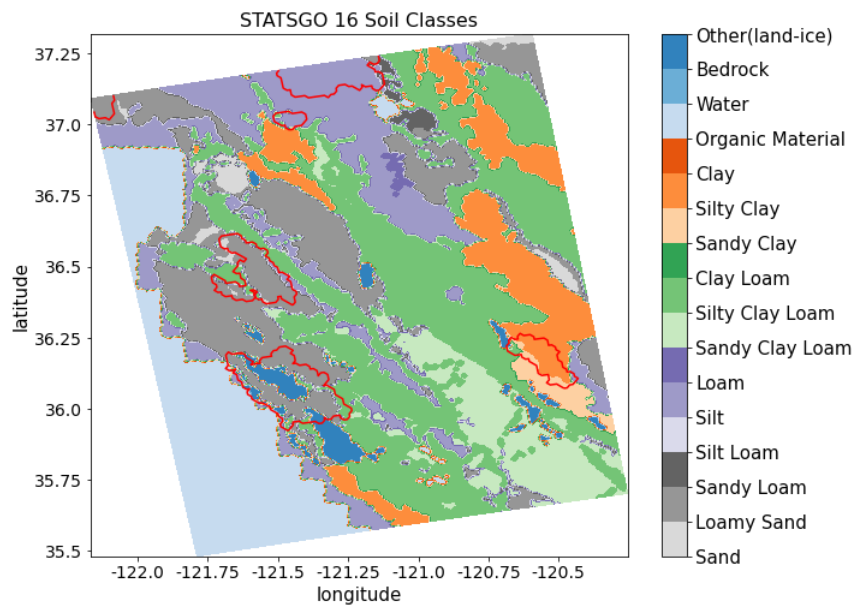
924



925 **Fig. B4** MODIS IGBP 20-category land cover type in the model domain. Red polylines are 2020
 926 wildfire burn scar perimeters.

927

928



929 **Fig. B5** 1-km STATSGO data with 16 soil texture types. Red polylines are 2020 wildfire burn
 930 scar perimeters.

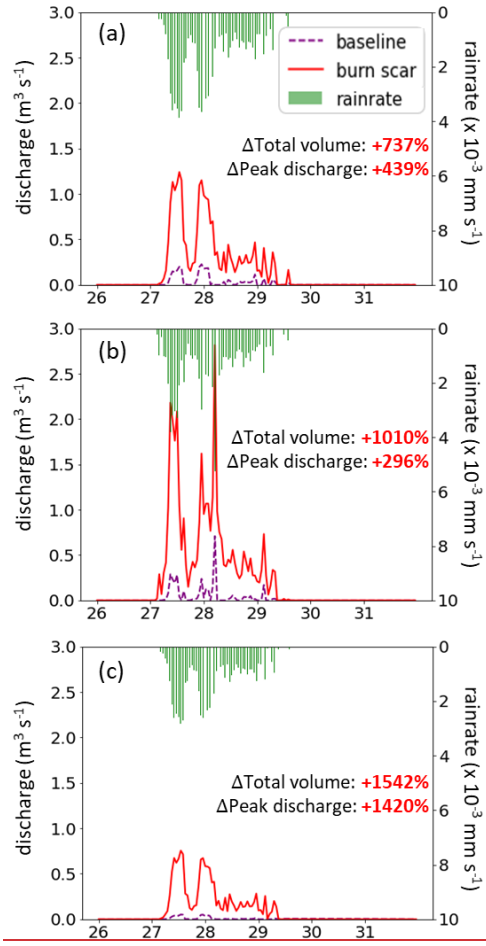
931
 932
 933
 934
 935

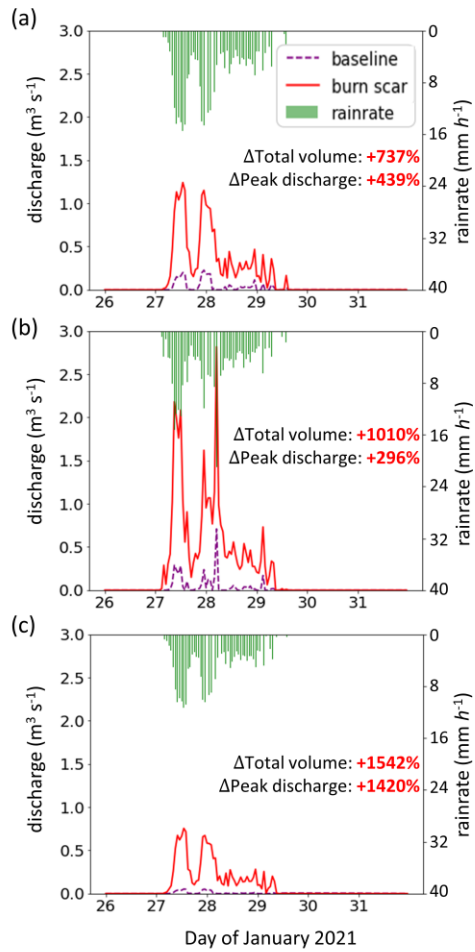
936 *Table B3*
 937 *Default and calibrated soil parameters in WRF-Hydro*
 938

Soil type	Default			After calibration		
	Grain size distribution index	Porosity	Saturated hydraulic conductivity (m s ⁻¹)	Grain size distribution index	Porosity	Saturated hydraulic conductivity (m s ⁻¹)
Sand	2.79	0.339	4.66E-5	2.51	0.315	1.5 x 10 ⁻⁷ m s ⁻¹ for all the burn scars, and original values elsewhere.
Loamy sand	4.26	0.421	1.41E-5	3.83	0.392	
Sandy loam	4.74	0.434	5.23E-6	4.27	0.404	
Silt loam	5.33	0.476	2.81E-6	4.80	0.442	
Silt	3.86	0.484	2.18E-6	3.47	0.450	
Loam	5.25	0.439	3.38E-6	4.73	0.408	
Sandy clay loam	6.77	0.404	4.45E-6	6.09	0.376	
Silty clay loam	8.72	0.464	2.03E-6	7.85	0.432	
Clay loam	8.17	0.465	2.45E-6	7.35	0.432	
Sandy clay	10.73	0.406	7.22E-6	9.66	0.378	
Silty clay	10.39	0.468	1.34E-6	9.35	0.435	
Clay	11.55	0.468	9.74E-7	10.40	0.435	
Organic material	5.25	0.439	3.38E-6	4.73	0.408	
Water	0.00	1.00	0.00	0.00	1.00	
Bedrock	2.79	0.200	1.41E-4	2.51	0.186	
Other	4.26	0.421	1.41E-5	3.83	0.392	
Playa	11.55	0.468	9.74E-7	10.40	0.435	
Lava	2.79	0.200	1.41E-4	2.51	0.186	
White sand	2.79	0.339	4.66E-5	2.51	0.315	

939 **Table B3** Soil parameters in default and calibrated WRF-Hydro. Default soil parameters in WRF-
 940 Hydro are adapted from the soil analysis by Cosby et al. (1984). Grain size distribution index and
 941 soil porosity are altered from default values during the global soil moisture calibration. Saturated
 942 hydraulic conductivity is altered from default values during the streamflow calibration.
 943
 944

945





947
 948
 949 **Fig. B6** WRF-Hydro simulated discharge time-series at four debris flow source areas. (a)–(c)
 950 MRMS precipitation (green bars) and simulated discharge time-series for January 26th 00:00 to
 951 31st 23:00 at Mill Creek, Big Creek, and Nacimientos debris flow source areas (black circles in Fig.
 952 7b–d) in baseline (purple dashed line) and burn scar simulation (red line).
 953
 954

955
 956
 957
 958
 959
 960

Table B4

The total runoff volume, peak discharge, and peak timing at debris-flow source areas

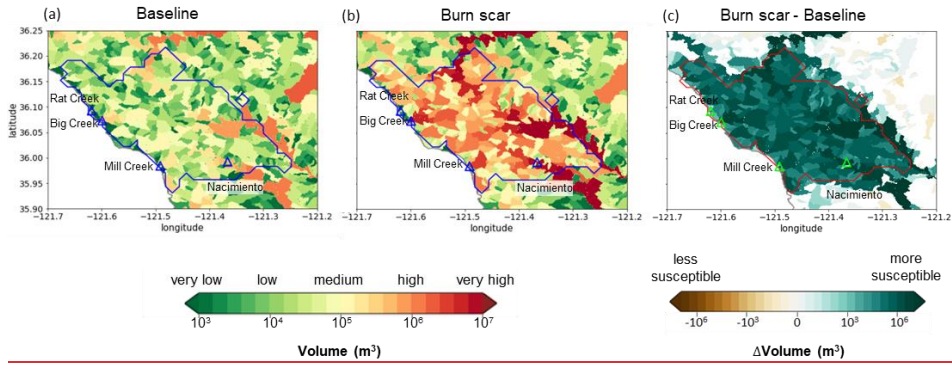
Site name	Baseline simulation			Burn scar simulation		
	Total volume (m ³)	Peak discharge (m ³ s ⁻¹)	Peak timing	Total volume (m ³)	Peak discharge (m ³ s ⁻¹)	Peak timing
Mill Creek	10,023	0.23	27 th 23:00	83,853 (+737%)	1.24 (+439%)	27 th 13:00
Big Creek	11,611	0.71	28 th 05:00	128,879 (+1010%)	2.81 (+296%)	28 th 05:00
Nacimiento	3,031	0.05	27 th 13:00	49,792 (+1542%)	0.76 (+1420%)	27 th 13:00

961
 962
 963
 964
 965
 966
 967
 968

Table B4 The total runoff volume, peak discharge, and peak timing in the baseline and burn scar simulations from January 27th 00:00 to 31st 23:00 at source areas of Rat Creek, Mill Creek, Big Creek, and Nacimiento debris flows (black circles in Fig. 7b–d). The percent change of the total volume and peak discharge in the burn scar simulation relative to the baseline simulation are shown in parentheses.

Formatted: Justified, Space After: 0 pt

Non-normalized catchment postfire debris flow susceptibility



969

970

971

972

973

974

975

976

977

978

979

980

981

982

983

984

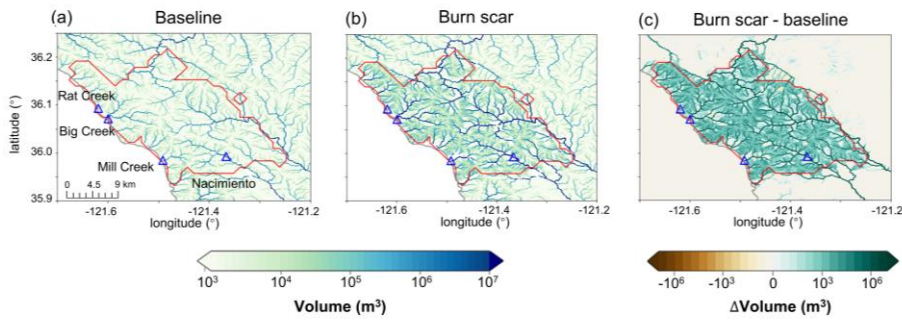
985

986

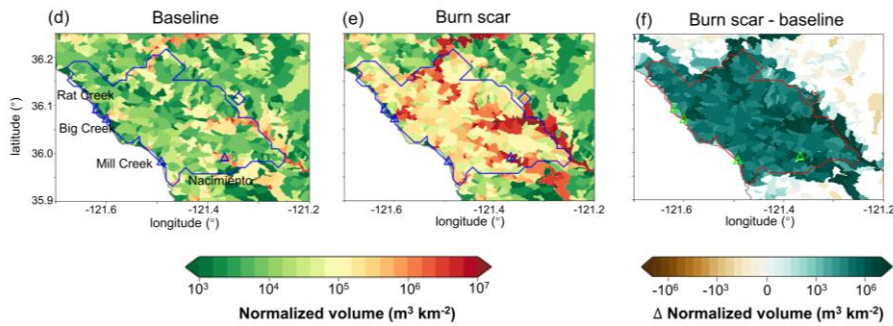
987

988

Stream channel accumulated discharge volume



Catchment-area normalized accumulated discharge volume



989
 990 **Fig. B7** ~~DischargeAccumulated discharge volume-based runoff generated debris flow~~
 991 ~~susceptibility at catchment/individual stream level infor~~ the (a) baseline ~~simulation~~, (b) burn scar
 992 ~~simulation~~, and (c) ~~the difference between the burn scar and baseline simulations-~~ (m³). Total
 993 ~~discharge volume is accumulated from January 27th 00:00 to 28th 12:00.~~ (d)–(f) Normalized
 994 ~~discharge volume by catchment area at catchment level (m³ km⁻²; shading; Santi & Morandi, 2013).~~
 995 For each catchment, the ~~susceptibility is assessed by computing the total discharge volume is~~
 996 ~~accumulated~~ at the catchment outlet from January 27th 00:00 to 28th 12:00 ~~divided by catchment~~
 997 ~~area. Triangles stand for debris flow deposition locations and are annotated in (a) and (d).~~

- Formatted: Font color: Black
- Formatted: Font color: Black
- Formatted: Font color: Black
- Formatted: Font color: Black
- Formatted: Font color: Black
- Formatted: Font color: Black
- Formatted: Font color: Black
- Formatted: Font color: Black

002
003
004

Table B5

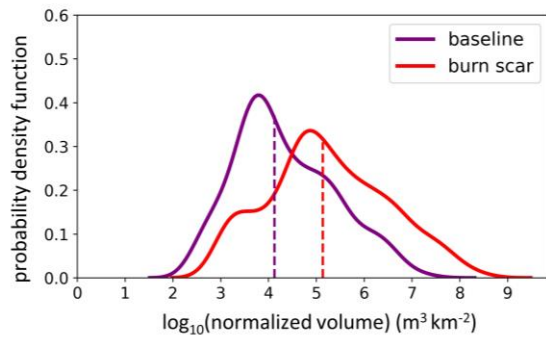
Statistics of catchment area-normalized discharge volume in baseline and burn scar simulations

	<u>mean</u>	<u>std</u>	<u>5P</u>	<u>25P</u>	<u>50P</u>	<u>75P</u>	<u>95P</u>
<u>Baseline simulation</u> (m ³ km ⁻²)	<u>380k</u>	<u>± 1.6M</u>	<u>0.6k</u>	<u>3.7k</u>	<u>13k</u>	<u>120k</u>	<u>2.1M</u>
<u>Burn scar simulation</u> (m ³ km ⁻²)	<u>5.5M</u>	<u>± 23.0M</u>	<u>1.5k</u>	<u>30.7k</u>	<u>135k</u>	<u>1.3M</u>	<u>29.1M</u>
<u>Relative percent change</u>	<u>1300%</u>	<u>1400%</u>	<u>148%</u>	<u>725%</u>	<u>924%</u>	<u>980%</u>	<u>1300%</u>

005 Table B5 Statistics, including the mean, standard deviation (std), 5P, 25P, 50P, 75P, and 95P, of
006 the catchment-area normalized discharge volume for all the 404 basins within the Dolan burn scar
007 in the baseline and burn scar simulation and their relative percent changes.

008
009
010
011
012
013
014
015

Distribution of catchment-area normalized volume



016

017 **Fig. B8** Distributions of accumulated discharge volumes at the outlet of the 404 catchments
018 normalized by upstream catchment areas within Dolan burn scar in the baseline simulation (purple
019 line) and in the burn scar simulation (red line). Dashed vertical lines indicate median values.

020

021

022

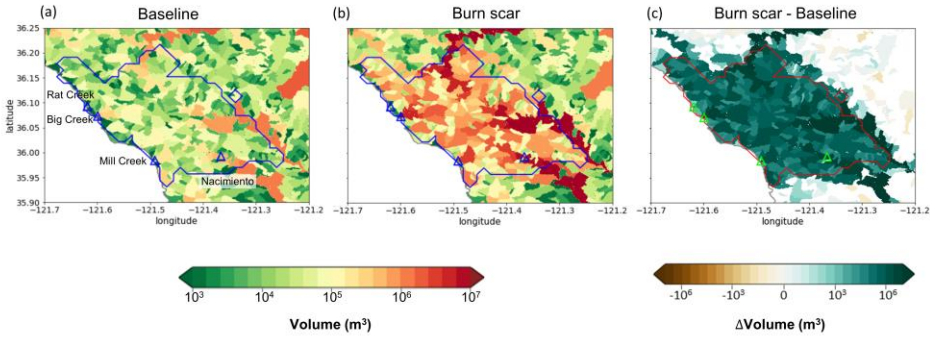
023

024

025

026

Non-normalized catchment accumulated discharge volume



027

028

029 **Fig. B9** Non-normalized accumulated discharge volume at catchment level in the (a) baseline
030 simulation, (b) burn scar simulation, and (c) the difference between the burn scar and baseline
031 simulations (m^3 ; shading). For each catchment, the discharge volume is accumulated at the
032 catchment outlet from January 27th 00:00 to 28th 12:00. Triangles stand for debris flow deposition
033 locations and are annotated in (a).

034

035

036

037

038

039

040

041

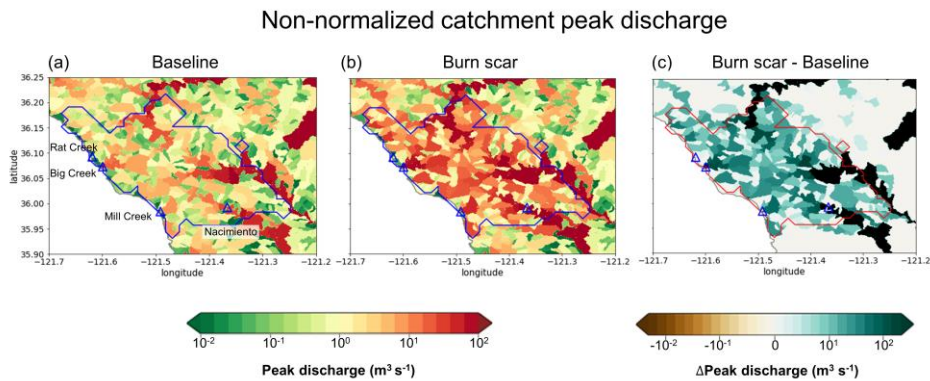


Fig. B10 Non-normalized peak discharge at catchment level in the (a) baseline simulation, (b) burn scar simulation, and (c) the difference between the burn scar and baseline simulations ($\text{m}^3 \text{s}^{-1}$; shading). For each catchment, the peak discharge is the maximum discharge rate at the catchment outlet from January 27th 00:00 to 28th 12:00. Triangles stand for debris flow deposition locations and are annotated in (a).

Formatted: Space Before: 0 pt, After: 0 pt, Border: Top: (No border), Bottom: (No border), Left: (No border), Right: (No border), Between : (No border)

Data availability statement

The NLDAS-2 reanalysis forcing data is publicly available at NASA GES DISC: <https://disc.gsfc.nasa.gov/datasets?keywords=NLDAS>. A detailed description can be found at <https://ldas.gsfc.nasa.gov/nldas/v2/forcing>. The MRMS radar-only precipitation estimate is publicly available at: <https://mtarchive.geol.iastate.edu/>. A description can be found at <https://www.nssl.noaa.gov/projects/mrms/>. The PSL in-situ soil moisture data is publicly available at: <https://psl.noaa.gov/data/obs/datadisplay/>. The USGS streamflow is publicly available at: <https://waterdata.usgs.gov/nwis/>. The wildfire perimeter shapefiles are downloadable at: <https://data-nifc.opendata.arcgis.com/search?collection=Dataset>. The remote sensing data used in this manuscript were provided by the European Space Agency (ESA) Copernicus program and accessed on Google Earth Engine (<https://code.earthengine.google.com>). All processed data required to reproduce the results of this study are archived on Zenodo at <http://doi.org/10.5281/zenodo.5544083>.

1066 **Code availability statement**

1067 The modified WRF-Hydro Fortran code and instructions to output the overland flow at terrain
1068 routing grid can be downloaded at <https://github.com/NU-CCRG/Modified-WRF-Hydro>.

1069 HazMapper v1.0 is available at <https://hazmapper.org/>. The SAR backscatter change method code
1070 is available at https://github.com/MongHanHuang/GEE_SAR_landslide_detection.

1071 **Author contribution**

1072 Conceptualization: CL, ALH, & DEH; Simulation and model analysis: CL; JW & WY model
1073 methodological development. Remote sensing analysis: ALH; Field Observations: NJF; GIS
1074 assistance: YX; Funding acquisition: GB & DH; CL wrote the original draft and all authors
1075 reviewed and edited the manuscript.

1076 **Competing interests**

1077 The authors declare that they have no conflict of interest.

1078 **Acknowledgments**

1079 C.L., A.L.H., J.W., X.L., G.B., and D.E.H. acknowledge support from NSF PREEVENTS
1080 #1848683. We acknowledge high-performance computing support from Cheyenne
1081 (doi:10.5065/D6RX99HX) provided by NCAR's Computational and Information Systems
1082 Laboratory, sponsored by the National Science Foundation. We thank P. Santi, an anonymous
1083 reviewer, and the editor for formal reviews, and F. K. Rengers for informal comments.
1084

1085

1086 **References**

1087 Alfieri L., Salamon P., Pappenberger F., Wetterhall F., Thielen J. (2012). Operational early warning systems for
1088 water-related hazards in Europe *Environmental Science & Policy* 21:35-49
1089 doi:<https://doi.org/10.1016/j.envsci.2012.01.008>

1090 Anderson, H. W., Hoover, M. D., & Reinhart, K. G. (1976). Forests and water: effects of forest management on
1091 floods, sedimentation, and water supply (Vol. 18): Department of Agriculture, Forest Service, Pacific
1092 Southwest Forest and Range Experiment Station, Berkeley, CA.

1093 Andersson, J. C. M., Arheimer, B., Traoré, F., Gustafsson, D., & Ali, A. (2017). Process refinements improve a
1094 hydrological model concept applied to the Niger River basin. *Hydrological Processes*, 31(25), 4540-
1095 4554. doi:<https://doi.org/10.1002/hyp.11376>

1096 [Anagnostou MN, Kalogiros J, Anagnostou EN, Tarolli M, Papadopoulos A, Borga MJJoh \(2010\) Performance](#)
1097 [evaluation of high-resolution rainfall estimation by X-band dual-polarization radar for flash flood](#)
1098 [applications in mountainous basins 394:4-16](#)

Formatted: Not Highlight

1099 Arattano, M., & Franzi, L. (2010). On the application of kinematic models to simulate the diffusive processes of
1100 debris flows. *Nat. Hazards Earth Syst. Sci.*, 10(8), 1689-1695. doi:10.5194/nhess-10-1689-2010

1101 Arattano, M., & Savage, W.Z. (1994). Modelling debris flows as kinematic waves. *Bulletin of the International
1102 Association of Engineering Geology* 49, 3–13. <https://doi.org/10.1007/BF02594995>

1103 Bart, R. (2016). A regional estimate of postfire streamflow change in California. *Water Resources Research*, 52,
1104 n/a-n/a. doi:10.1002/2014WR016553

1105 Bart, R., & Hope, A. (2010). Streamflow response to fire in large catchments of a Mediterranean-climate region
1106 using paired-catchment experiments. *Journal of Hydrology*, 388, 370-378.
1107 doi:10.1016/j.jhydrol.2010.05.016

1108 [Barth NA, Villarini G, Nayak MA, White K \(2017\) Mixed populations and annual flood frequency estimates in
1109 the western United States: The role of atmospheric rivers *Water Resour Res* 53:257-269](#)

1110 Brabb E.E. (1985) Innovative approaches to landslide hazard and risk mapping. In: *International Landslide
1111 Symposium Proceedings*, Toronto, Canada. pp 17-22

1112 Bisson M., Favalli M., Fornaciai A., Mazzarini F., Isola I., Zanchetta G., & Pareschi M.T. (2005). A rapid method
1113 to assess fire-related debris flow hazard in the Mediterranean region: An example from Sicily (southern
1114 Italy) *International Journal of Applied Earth Observation and Geoinformation* 7:217-231
1115 doi:<https://doi.org/10.1016/j.jag.2005.04.003>

1116 Bitew, M. M., & Gebremichael, M. (2011). Assessment of satellite rainfall products for streamflow simulation
1117 in medium watersheds of the Ethiopian highlands. *Hydrol. Earth Syst. Sci.*, 15(4), 1147-1155.
1118 doi:10.5194/hess-15-1147-2011

1119 Brown, E.K., Wang, J., & Feng, Y. (2020). U.S. wildfire potential: a historical view and future projection using
1120 high-resolution climate data. *Environmental Research Letters*. 16, 034060

1121 Brunkal, H., & Santi, P. M. (2016). Exploration of design parameters for a dewatering structure for debris flow
1122 mitigation. 208, 81-92.

1123 Bytheway, J. L., Hughes, M., Mahoney, K., & Cifelli, R. (2020). On the Uncertainty of High-Resolution Hourly
1124 Quantitative Precipitation Estimates in California, *Journal of Hydrometeorology*, 21(5), 865-879.
1125 Retrieved Oct 25, 2021, from [https://journals.ametsoc.org/view/journals/hydr/21/5/jhm-d-19-
1126 0160.1.xml](https://journals.ametsoc.org/view/journals/hydr/21/5/jhm-d-19-0160.1.xml)

1127 Canfield, H. E., Goodrich, D. C., & Burns, I. S. (2005). Selection of parameters values to model post-fire runoff
1128 and sediment transport at the watershed scale in southwestern forests. In *Managing watersheds for
1129 human and natural impacts: engineering, ecological, and economic challenges* (pp. 1-12).

1130 Canli E., Mergili M., Thiebes B., & Glade T. (2018) Probabilistic landslide ensemble prediction systems: lessons
1131 to be learned from hydrology *Nat Hazards Earth Syst Sci* 18:2183-2202 doi:10.5194/nhess-18-2183-
1132 2018

1133 Cannon, S.H., Kirkham R.M., & Paise M., (2001). Wildfire-related debris-flow initiation processes, Storm King
1134 Mountain, Colorado. *Geomorphology*, v.39, n. 3-4, 171-188

1135 Cannon, S. H., Gartner, J. E., Parrett, C., & Parise, M. (2003). Wildfire-related debris-flow generation through
1136 episodic progressive sediment-bulking processes, western USA. *Debris-Flow Hazards Mitigation:
1137 Mechanics, Prediction, and Assessment*. Millpress, Rotterdam, pp. 71-82.

1138 Cannon, S. H., Gartner, J., Wilson, R., Bowers, J., & Laber, J. (2008). Storm Rainfall Conditions for Floods and
1139 Debris Flows from Recently Burned Basins in Southwestern Colorado and Southern California. *Geomorphology*, 96, 250-269. Doi:10.1016/j.geomorph.2007.03.019

1140 Cannon, S. H., & DeGraff, J. (2009). The increasing wildfire and postfire debris flow threat in western USA,
1141 and implications for consequences of climate change. In *Landslides—disaster risk reduction* (pp. 177-
1142 190): Springer.

1144 Cannon, S. H., Gartner, J. E., Rupert, M. G., Michael, J. A., Rea, A. H., & Parrett, C. (2010). Predicting the
1145 probability and volume of postwildfire debris flows in the intermountain western United States. *GSA*
1146 *Bulletin*, 122(1-2), 127-144. Doi:10.1130/B26459.1

1147 Cannon, S. H., Boldt, E. M., Laber, J. L., Kean, J. W., & Staley, D. M. J. N. H. (2011). Rainfall intensity–
1148 duration thresholds for postfire debris flow emergency-response planning. *59*(1), 209-236.

1149 Cavagnaro, D. et al. (2021) Variability in hydrologic response to rainfall across a burn scar: observations from
1150 the Dolan Fire, California. AGU abstract.
1151 <https://agu.confex.com/agu/fm21/meetingapp.cgi/Paper/921613>

1152 Cerdà, A. (1998). Changes in overland flow and infiltration after a rangeland fire in a Mediterranean scrubland.
1153 *Hydrological Processes*, 12(7), 1031-1042. Doi:[https://doi.org/10.1002/\(SICI\)1099-1085\(19980615\)12:7<1031::AID-HYP636>3.0.CO;2-V](https://doi.org/10.1002/(SICI)1099-1085(19980615)12:7<1031::AID-HYP636>3.0.CO;2-V)

1154 Chen, F., & Dudhia, J. (2001). Coupling an Advanced Land Surface–Hydrology Model with the Penn State–
1155 NCAR MM5 Modeling System. Part I: Model Implementation and Sensitivity, *Monthly Weather*
1156 *Review*, 129(4), 569-585. Retrieved Oct 24, 2021, from
1157 https://journals.ametsoc.org/view/journals/mwre/129/4/1520-0493_2001_129_0569_caalsh_2.0.co_2.xml

1160 Chen, L., Berli, M., & Chief, K. (2013). Examining Modeling Approaches for the Rainfall-Runoff Process in
1161 Wildfire-Affected Watersheds: Using San Dimas Experimental Forest. *JAWRA Journal of the*
1162 *American Water Resources Association*, 49(4), 851-866. Doi:<https://doi.org/10.1111/jawr.12043>

1163 Claessens L., Schoolj, J.M., & Veldkamp, A. (2007) Modelling the location of shallow landslides and their
1164 effects on landscape dynamics in large watersheds: An application for Northern New Zealand
1165 *Geomorphology* 87:16-27 doi:<https://doi.org/10.1016/j.geomorph.2006.06.039>

1166 Crosta G. B., & Fratini P. (2003) Distributed modelling of shallow landslides triggered by intense rainfall. *Nat*
1167 *Hazards Earth Syst Sci* 3:81-93 doi:10.5194/nhess-3-81-2003

1168 Cui, Y., Cheng, D., & Chan, D. (2018). Investigation of post-fire debris flows in Montecito. *ISPRS International*
1169 *Journal of Geo-Information*, 8(1), 5.

1170 Coe, J., Godt, J., Parise, M., & Moscarillo, A. (2003). Estimating debris flow probability using fan stratigraphy,
1171 historic records, and drainage-basin morphology, Interstate 70 highway corridor, central Colorado, USA.
1172 Paper presented at the Debris flow Hazards Mitigation: Mechanics, Prediction, and Assessment, edited
1173 by: Rickenmann, D. and Cheng, Ch., *Proceedings 3rd International DFHM Conference*, Davos,
1174 Switzerland.

1175 Coe, J. A., Kinner, D. A., & Godt, J. W. J. G. (2008). Initiation conditions for debris flows generated by runoff
1176 at Chalk Cliffs, central Colorado. *96*(3-4), 270-297.

1177 [Collow ABM, Mersiovsky H, Bosilovich MG \(2020\) Large-Scale Influences on Atmospheric River-Induced](#)
1178 [Extreme Precipitation Events along the Coast of Washington State J Hydrometeor 21:2139-2156](#)
1179 [doi:10.1175/JHM-D-19-0272.1](#)

1180 Cosby, B. J., Hornberger, G. M., Clapp, R. B., & Ginn, T. R. (1984). A Statistical Exploration of the
1181 Relationships of Soil Moisture Characteristics to the Physical Properties of Soils. *Water Resources*
1182 *Research*, 20(6), 682-690. Doi:<https://doi.org/10.1029/WR020i006p00682>

1183 Cydzik, K., & Hogue, T. S. (2009). Modeling postfire response and recovery using the hydrologic engineering
1184 center hydrologic modeling system (HEC-HMS) 1. *JAWRA Journal of the American Water Resources*
1185 *Association*, 45(3), 702-714.

1186 Dahal, R.K., Hasegawa, S., Nonomura, A., Yamanaka, M., Dhakal, S., Paudyal, P. (2008) Predictive modelling
1187 of rainfall-induced landslide hazard in the Lesser Himalaya of Nepal based on weights-of-evidence
1188 *Geomorphology* 102:496-510 doi:<https://doi.org/10.1016/j.geomorph.2008.05.041>

1189 Daly, C., R. P. Neilson, & D. L. Phillips. (1994). A statistical-topographic model for mapping climatological
1190 precipitation over mountainous terrain. *J. Appl. Meteor.*, 33, 140–147. doi:10.1029/1993-1002joc.4986.
1191 Daly, C., M. E. Slater, J. A. Roberti, S. H. Laseter, & L. W. Swift Jr. (2017). High-resolution precipitation
1192 mapping in a mountainous watershed; Ground truth for evaluating uncertainty in a national precipitation
1193 dataset. *Int. J. Climatol.*, 37, 124–137, <https://doi.org/10.1002/joc.4986>.
1194 Davies, T., Phillips, C., Pearce, A., & Zhang, X. J. I. P. (1992). Debris flow behaviour—an integrated overview.
1195 *209(21)*, 225.
1196 Dekker, L. W., & Ritsema, C. J. (1994). How water moves in a water repellent sandy soil: 1. Potential and actual
1197 water repellency. *Water Resources Research*, 30(9), 2507-2517.
1198 Doi:<https://doi.org/10.1029/94WR00749>
1199 Deser, C. et al. (2020) Insights from Earth system model initial-condition large ensembles and future prospects
1200 *Nature Climate Change* 10:277-286 doi:10.1038/s41558-020-0731-2
1201 Di Cristo, C., Iervolino, M., Moramarco, T., & Vacca, A. (2021). Applicability of Diffusive model for mud-
1202 flows: An unsteady analysis. *Journal of Hydrology*, 600, 126512.
1203 Doi:<https://doi.org/10.1016/j.jhydrol.2021.126512>
1204 Doerr, S. H., & Thomas, A. (2000). The role of soil moisture in controlling water repellency: New evidence
1205 from forest soils in Portugal. *Journal of Hydrology*, 231-232, 134-147. Doi:10.1016/S0022-
1206 1694(00)00190-6
1207 [Eldardiry H, Mahmood A, Chen X, Hossain F, Nijssen B, Lettenmaier DP \(2019\) Atmospheric River-Induced](#)
1208 [Precipitation and Snowpack during the Western United States Cold Season J Hydrometeor 20:613-630](#)
1209 [doi:10.1175/JHM-D-18-0228.1](#)
1210 Flannigan, M., Cantin, A. S., De Groot, W. J., Wotton, M., Newbery, A., & Gowman, L. M. (2013). Global
1211 wildland fire season severity in the 21st century. *Forest Ecology and Management*, 294, 54-61.
1212 Friedel, M.J. (2011a). A data-driven approach for modeling post-fire debris-flow volumes and their uncertainty
1213 *Environmental Modelling & Software* 26:1583-1598 doi:<https://doi.org/10.1016/j.envsoft.2011.07.014>
1214 Friedel, M.J. (2011b) Modeling hydrologic and geomorphic hazards across post-fire landscapes using a self-
1215 organizing map approach *Environmental Modelling & Software* 26:1660-1674
1216 doi:<https://doi.org/10.1016/j.envsoft.2011.07.001>
1217 Gartner, J. E., Cannon, S. H., & Santi, P. M. (2014). Empirical models for predicting volumes of sediment
1218 deposited by debris flows and sediment-laden floods in the transverse ranges of southern California.
1219 *Engineering Geology*, 176, 45-56. doi:<https://doi.org/10.1016/j.enggeo.2014.04.008>
1220 George, D. L., & Iverson, R. M. (2014). A depth-averaged debris flow model that includes the effects of evolving
1221 dilatancy. II. Numerical predictions and experimental tests. *Proceedings of the Royal Society A: Mathematical, Physical and Engineering Sciences*, 470(2170), 20130820. doi:10.1098/rspa.2013.0820
1222 [Germann U, Galli G, Boscacci M, Bolliger M \(2007\) Radar Precipitation Measurement in a Mountainous Region](#)
1223 [Q J Roy Meteorol Soc 132:1669-1692 doi:10.1256/qj.05.190](#)
1224 Gochis, D. J., & Chen, F. (2003). Hydrological Enhancements to the Community Noah Land Surface Model (No.
1225 NCAR/TN-454+STR). University Corporation for Atmospheric Research. doi:10.5065/D60P0X00
1226 Goodrich, D., Burns, I., Unkrich, C., Semmens, D., Guertin, D., Hernandez, M., . . . Levick, L. (2012).
1227 KINEROS2/AGWA: model use, calibration, and validation. *Transactions of the ASABE*, 55, 1561-
1228 1574. doi:10.13031/2013.42264
1230 Goss, M., Swain, D. L., Abatzoglou, J. T., Sarhadi, A., Kolden, C. A., Williams, A. P., & Duffenbaugh, N. S.
1231 (2020). Climate change is increasing the likelihood of extreme autumn wildfire conditions across
1232 California. *Environmental Research Letters*, 15(9), 094016. doi:10.1088/1748-9326/ab83a7

Formatted: Not Highlight

1233 Gregoretti, C., & Dalla Fontana, G. (2007). Rainfall threshold for the initiation of debris flows by channel-bed
1234 failure in the Dolomites. *Debris-Flow Hazards Mitigation: Mechanics, Prediction, and Assessment*, 11-
1235 22.

1236 Gregoretti, C., & Dalla Fontana, G. (2008). The triggering of debris flow due to channel-bed failure in some
1237 alpine headwater basins of the Dolomites: analyses of critical runoff. *Hydrological Processes*, 22(13),
1238 2248-2263. doi:<https://doi.org/10.1002/hyp.6821>

1239 Gupta, H. V., Kling, H., Yilmaz, K. K., & Martinez, G. F. (2009). Decomposition of the mean squared error and
1240 NSE performance criteria: Implications for improving hydrological modelling. *Journal of Hydrology*,
1241 377(1), 80-91. doi:<https://doi.org/10.1016/j.jhydrol.2009.08.003>

1242 Guzzetti, F., Reichenbach, P., Cardinali, M., Galli, M., & Ardizzone, F. J. G. (2005) Probabilistic landslide
1243 hazard assessment at the basin scale *72:272-299*

1244 Handwerker, ~~A. L., AL~~, Huang, ~~M. H., MH~~, Jones, ~~S. Y., SY~~, Amatya, ~~P., Kerner, H. R., and HR~~, Kirschbaum,
1245 ~~D. B., DB~~ (2022) Generating landslide density heatmaps for rapid detection using open-access satellite
1246 radar data in Google Earth Engine. *Nat. Hazards Earth Syst. Sci.—Discuss.*, ~~22:753-773~~
1247 doi:[10.5194/nhess-2021-28322-753-2022](https://doi.org/10.5194/nhess-2021-28322-753-2022)

1248 Hapuarachchi, H.A.P., Wang, Q.J., & Pagano, T.C. (2011) A review of advances in flash flood forecasting.
1249 *Hydrological processes*. 25:2771-2784 doi:<https://doi.org/10.1002/hyp.8040>

1250 Hawkins, E., Sutton, R. (2009) The Potential to Narrow Uncertainty in Regional Climate Predictions *Bull Amer*
1251 *Meteor Soc* 90:1095-1108 doi:[10.1175/2009BAMS2607.1](https://doi.org/10.1175/2009BAMS2607.1)

1252 ~~Huang, X., Swain, D. L., & Hall, A. D. (2020)~~ ~~Hecht, C. W., & Cordeira, J. M. (2017). Characterizing the~~
1253 ~~influence of atmospheric river orientation and intensity on precipitation distributions over North Coastal~~
1254 ~~California. *Geophysical Research Letters*, 44(17), 9048-9058.~~

1255 ~~Huang X., Stevenson, S., Hall, A.D. (2020a) Future warming and intensification of precipitation extremes: A~~
1256 ~~“double whammy” leading to increasing flood risk in California. *Geophysical Research Letters*,~~
1257 ~~47:e2020GL088679~~

1258 ~~Huang X., Swain D.L., Hall A.D. (2020b) Future precipitation increase from very high resolution ensemble~~
1259 ~~downscaling of extreme atmospheric river storms in California:___ 6(29),—;eaba1323-~~
1260 ~~doi:10.1126/sciadv.aba1323 %J Science *Advances*~~

1261 ~~IceAdvancesIce~~, G. G., Neary, D. G., & Adams, P. W. (2004). Effects of Wildfire on Soils and Watershed
1262 Processes. *Journal of Forestry*, 102(6), 16-20. doi:[10.1093/jof/102.6.16](https://doi.org/10.1093/jof/102.6.16)

1263 Iverson, R. M., & George, D. L. (2014). A depth-averaged debris flow model that includes the effects of evolving
1264 dilatancy. I. Physical basis. *Proceedings of the Royal Society A: Mathematical, Physical and*
1265 *Engineering Sciences*, 470(2170), 20130819. doi:[10.1098/rspa.2013.0819](https://doi.org/10.1098/rspa.2013.0819)

1266 Jolly, W. M., Cochrane, M. A., Freeborn, P. H., Holden, Z. A., Brown, T. J., Williamson, G. J., & Bowman, D.
1267 M. J. S. (2015). Climate-induced variations in global wildfire danger from 1979 to 2013. *Nature*
1268 *Communications*, 6(1), 7537. doi:[10.1038/ncomms8537](https://doi.org/10.1038/ncomms8537)

1269 Julien, P. Y., Saghafian, B., & Ogden, F. L. (1995). RASTER-BASED HYDROLOGIC MODELING OF
1270 SPATIALLY-VARIED SURFACE RUNOFF1. *JAWRA Journal of the American Water Resources*
1271 *Association*, 31(3), 523-536. doi:<https://doi.org/10.1111/j.1752-1688.1995.tb04039.x>

1272 Kean, J. W., Staley, D. M., & Cannon, S. H. (2011). In situ measurements of postfire debris flows in southern
1273 California: Comparisons of the timing and magnitude of 24 debris flow events with rainfall and soil
1274 moisture conditions. *Journal of Geophysical Research F: Earth Surface*, 116(4).
1275 doi:[10.1029/2011JF002005](https://doi.org/10.1029/2011JF002005)

1276 Kean, J. W., McCoy, S. W., Tucker, G. E., Staley, D. M., & Coe, J. A. (2013). Runoff-generated debris flows:
1277 Observations and modeling of surge initiation, magnitude, and frequency. *Journal of Geophysical*
1278 *Research: Earth Surface*, 118(4), 2190-2207. doi:<https://doi.org/10.1002/jgrf.20148>

1279 Kean, J. W., & Staley, D. M. (2021). Forecasting the Frequency and Magnitude of Postfire Debris Flows Across
1280 Southern California. *Earth's Future*, 9(3), e2020EF001735. doi:<https://doi.org/10.1029/2020EF001735>

1281 Kinoshita, A. M., & Hogue, T. S. (2015). Increased dry season water yield in burned watersheds in Southern
1282 California. *Environmental Research Letters*, 10(1), 014003. doi:10.1088/1748-9326/10/1/014003

1283 Kling, H., Fuchs, M., & Paulin, M. (2012). Runoff conditions in the upper Danube basin under an ensemble of
1284 climate change scenarios. *Journal of Hydrology*, 424-425, 264-277.
1285 doi:<https://doi.org/10.1016/j.jhydrol.2012.01.011>

1286 Larsen, I., MacDonald, L., Brown, E., Rough, D., Welsh, M., Pietraszek, J., . . . Schaffrath, K. (2009). Causes
1287 of Postfire Runoff and Erosion: Water Repellency, Cover, or Soil Sealing? *Soil Science Society of
1288 America Journal - SSSAJ*, 73. doi:10.2136/sssaj2007.0432

1289 Lahmers, T. M., Gupta, H., Castro, C. L., Gochis, D. J., Yates, D., Dugger, A., . . . Hazenberg, P. J. J. o. H.
1290 (2019). Enhancing the structure of the WRF-Hydro hydrologic model for semiarid environments. 20(4),
1291 691-714.

1292 Lahmers, T. M., Castro, C. L., & Hazenberg, P. (2020). Effects of Lateral Flow on the Convective Environment
1293 in a Coupled Hydrometeorological Modeling System in a Semiarid Environment, *Journal of
1294 Hydrometeorology*, 21(4), 615-642. Retrieved Sep 29, 2021, from
1295 [https://journals.ametsoc.org/view/journals/hydr/21/4/jhm-d-19-
1296 0100-1.xml](https://journals.ametsoc.org/view/journals/hydr/21/4/jhm-d-19-0100-1.xml)<https://journals.ametsoc.org/view/journals/hydr/21/4/jhm-d-19-0100-1.xml>

1297 Leopold, L. B., M. G. Wolman, and J.P. Miller. *Fluvial Processes in Geomorphology*. W. H. Freeman, New
1298 York, 1964

1299 MacDonald, L. H., & Huffman, E. L. (2004). Postfire soil water repellency: Persistence and soil moisture
1300 thresholds. *Soil Science Society of America Journal*, 68, 1729-1734.

1301 Martin, D., & Moody, J. (2001). Comparison of Soil Infiltration Rates in Burned and Unburned Mountainous
1302 Watersheds. *Hydrological Processes*, 15, 2893-2903. doi:10.1002/hyp.380

1303 McCormick, B. C., Eshleman, K. N., Griffith, J. L., & Townsend, P. A. (2009). Detection of flooding responses
1304 at the river basin scale enhanced by land use change. *Water Resour. Res.*, 45, W08401,
1305 doi:10.1029/2008WR007594.

1306 ~~McGuire, L. A., J. W. Kean, D. M. J. W., Staley, F. K. D. M., Rengers, and T. A. F. K., & Wasklewicz, T. A.~~
1307 ~~(2016-). Constraining the relative importance of raindrop- and flow-driven sediment transport
1308 mechanisms in postwildfire environments and implications for recovery time scales, *J. Geophys. Res.*
1309 *Earth Surf.*, 121, 2211– 2237, doi:10.1002/2016JF003867~~

1310 McGuire, L. A., Rengers, F. K., Kean, J. W., & Staley, D. M. (2017). Debris flow initiation by runoff in a
1311 recently burned basin: Is grain-by-grain sediment bulking or en masse failure to blame? *Geophysical
1312 Research Letters*, 44(14), 7310-7319. doi:<https://doi.org/10.1002/2017GL074243>

1313 McGuire, L. A., & Youberg, A. M. (2020). What drives spatial variability in rainfall intensity-duration thresholds
1314 for post-wildfire debris flows? Insights from the 2018 Buzzard Fire, NM, USA. *Landslides*, 17(10),
1315 2385-2399. doi:10.1007/s10346-020-01470-y

1316 McMichael, C. E., & Hope, A. S. (2007). Predicting streamflow response to fire-induced landcover change:
1317 implications of parameter uncertainty in the MIKE SHE model. *J Environ Manage*, 84(3), 245-256.
1318 doi:10.1016/j.jenvman.2006.06.003

1319 Neiman, P. J., Ralph, F. M., Wick, G. A., Lundquist, J. D., & Dettinger, M. D. (2008). Meteorological
1320 Characteristics and Overland Precipitation Impacts of Atmospheric Rivers Affecting the West Coast of
1321 North America Based on Eight Years of SSM/I Satellite Observations, *Journal of Hydrometeorology*,
1322 9(1), 22-47. Retrieved May 13, 2022, from
1323 https://journals.ametsoc.org/view/journals/hydr/9/1/2007jhm855_1.

Formatted: Font: 10 pt

1324 Meixner, T., & Wohlgemuth, P. M. (2003). Climate variability, fire, vegetation recovery, and watershed
1325 hydrology. In Proceedings of the First Interagency Conference on Research in the Watersheds, Benson,
1326 Arizona (pp. 651-656).

1327 Meyer, G. A., & Wells, S. G. (1997). Fire-related sedimentation events on alluvial fans, Yellowstone National
1328 Park, U.S.A. *Journal of Sedimentary Research*, 67(5), 776-791. doi:10.1306/D426863A-2B26-11D7-
1329 8648000102C1865D

1330 Miller, D. A., & White, R. A. (1998). A Conterminous United States Multilayer Soil Characteristics Dataset for
1331 Regional Climate and Hydrology Modeling, *Earth Interactions*, 2(2), 1-26. Retrieved Sep 27, 2021, from
1332 https://journals.ametsoc.org/view/journals/eint/2/2/1087-3562_1998_002_0001_acusms_2.3.co_2.xml

1333 Mitsopoulos, I. D., & Mironidis, D. (2006). Assessment of post fire debris flow potential in a Mediterranean
1334 type ecosystem. *WIT Transactions on Ecology and the Environment*, 90.

1335 Moody, J. A., Shakesby, R. A., Robichaud, P. R., Cannon, S. H., & Martin, D. A. (2013). Current research issues
1336 related to post-wildfire runoff and erosion processes. *Earth-Science Reviews*, 122, 10-37.
1337 doi:<https://doi.org/10.1016/j.earscirev.2013.03.004>

1338 Moriasi, D. N., Arnold, J. G., Van Liew, M. W., Bingner, R. L., Harmel, R. D., & Veith, T. L. (2007). Model
1339 evaluation guidelines for systematic quantification of accuracy in watershed simulations. *Transactions*
1340 *of the ASABE*, 50(3), 885-900.

1341 Nash, J. E., & Sutcliffe, J. V. (1970). River flow forecasting through conceptual models part I — A discussion
1342 of principles. *Journal of Hydrology*, 10(3), 282-290. doi:[https://doi.org/10.1016/0022-1694\(70\)90255-](https://doi.org/10.1016/0022-1694(70)90255-6)
1343 6

1344 Neary, D. G., Gottfried, G. J., & Ffolliott, P. F. (2003). Post-wildfire watershed flood responses. In Proceedings
1345 of the 2nd International Fire Ecology Conference, Orlando, Florida (pp. 16-20).

1346 Nikolopoulos, E.I., Destro, E., Bhuiyan, M.A.E, Borga, M., & Anagnostou, E.N. (2018). Evaluation of predictive
1347 models for postfire debris flow occurrence in the western United States *Nat Hazards Earth Syst Sci*
1348 18:2331-2343 doi:10.5194/nhess-18-2331-2018

1349 Nikolopoulos, E.I., Schwartz, C., Zhang, X, & Anagnostou, E.N. (2019) Rainfall estimation uncertainty and
1350 early warning procedures for post-fire debris flows. In: *Geophysical Research Abstracts*.

1351 Niu, G-Y et al. (2011) The community Noah land surface model with multiparameterization options (Noah-MP):
1352 1. Model description and evaluation with local-scale measurements *J Geophys Res Atm* 116
1353 doi:<https://doi.org/10.1029/2010JD015139>

1354 Nyman, P., Smith, H.G., Sherwin, C.B., Langhans, C., Lane, P.N. J., & Sheridan, G.J. (2015). Predicting
1355 sediment delivery from debris flows after wildfire. *Geomorphology*, 250, 173-186.
1356 doi:<https://doi.org/10.1016/j.geomorph.2015.08.023>

1357 [Oakley N.S., Lancaster J.T., Kaplan M.L., Ralph F.M. \(2017\) Synoptic conditions associated with cool season](#)
1358 [post-fire debris flows in the Transverse Ranges of southern California *Nat Hazards* 88:327-354](#)
1359 [doi:10.1007/s11069-017-2867-6](#)

1360 [Oakley N.S., Cannon F., Munroe R., Lancaster J.T., Gomberg D., Ralph F.M. \(2018\) Brief Communication:](#)
1361 [Meteorological and climatological conditions associated with the 9 January 2018 post-fire debris flows](#)
1362 [in Montecito and Carpinteria, California, USA *Nat Hazards Earth Syst Sci* 18:3037-3043](#)
1363 [doi:10.5194/nhess-18-3037-2018](#)

1364 Oakley, N.S. (2021). A warming climate adds complexity to postfire hydrologic hazard planning. *Earth's Future*,
1365 9, e2021EF002149. <https://doi.org/10.1029/2021EF002149><https://doi.org/10.1029/2021EF002149>

1366 Ogden, F.L. (1997). CASC2D reference manual. Department of Civil & Environmental Engineering, University
1367 of Connecticut, Storrs.

1368 Palmer, J. (2022). The devastating mudslides that follow forest fires. *Nature*.
1369 <https://www.nature.com/articles/d41586-022-00028-3>.

1370 Parise, M., & Cannon, S.H. (2008) The effects of wildfires on erosion and debris-flow generation in
1371 Mediterranean climatic areas: a first database. Proceedings of 1st World Landslide Forum. Tokyo, Japan,
1372 pp 465–468

1373 Parise, M., & Cannon, S.H. (2009). A database on post-fire erosion rates and debris flows in Mediterranean-
1374 Basin watersheds. EGU General Assembly, Abstracts, p. 1530.

1375 Parise, M., & Cannon, S.H. (2012) Wildfire impacts on the processes that generate debris flows in burned
1376 watersheds *Nat Hazards* 61:217-227 doi:10.1007/s11069-011-9769-9

1377 Park, D.W., Lee, S.R., Vasu, N.N., Kang, S.H., Park, J.Y. (2016) Coupled model for simulation of landslides
1378 and debris flows at local scale *Nat Hazards* 81:1653-1682 doi:10.1007/s11069-016-2150-2

1379 Polade, S.D., Gershunov, A., Cayan, D.R., Dettinger, M.D., & Pierce, D.W. (2017) Precipitation in a warming
1380 world: Assessing projected hydro-climate changes in California and other Mediterranean climate
1381 regions *Scientific Reports* 7:10783 doi:10.1038/s41598-017-11285-y

1382 Qi, Y., Martinaitis, S., Zhang, J., & Cocks, S. (2016). A real-time automated quality control of hourly rain gauge
1383 data based on multiple sensors in MRMS system. *J. Hydrometeor.*, 17, 1675–1691,
1384 <https://doi.org/10.1175/JHM-D-15-0188.1>.

1385 Raia, S., Alvioli, M., Rossi, M., Baum, R. L., Godt, J.W., & Guzzetti, F. (2014) Improving predictive power of
1386 physically based rainfall-induced shallow landslide models: a probabilistic approach *Geosci Model Dev*
1387 7:495-514 doi:10.5194/gmd-7-495-2014

1388 [Ralph, F. M., Neiman, P. J., & Wick, G. A. \(2004\) Satellite and CALJET aircraft observations of atmospheric
1389 rivers over the eastern North Pacific Ocean during the winter of 1997/98. *Mon. Wea. Rev.*, 132, 1721–
1390 1745. \[https://doi.org/10.1175/1520-0493\\(2004\\)132<1721:SACAOO>2.0.CO;2\]\(https://doi.org/10.1175/1520-0493\(2004\)132<1721:SACAOO>2.0.CO;2\).](https://doi.org/10.1175/1520-0493(2004)132<1721:SACAOO>2.0.CO;2)

1391 Regmi, N.R., Giardino, J.R., Vittek, J.D. (2010) Modeling susceptibility to landslides using the weight of
1392 evidence approach: Western Colorado, USA *Geomorphology* 115:172-187
1393 doi:<https://doi.org/10.1016/j.geomorph.2009.10.002>

1394 Reichenbach, P., Rossi, M., Malamud, B.D., Mihir, M., & Guzzetti, F. (2018) A review of statistically-based
1395 landslide susceptibility models *Earth-Science Reviews* 180:60-91
1396 doi:<https://doi.org/10.1016/j.earscirev.2018.03.001>

1397 Rengers, F.K., McGuire, L.A., Kean, J.W., Staley, D.M., & Hobley, D.E.J. (2016). Model simulations of flood
1398 and debris flow timing in steep catchments after wildfire. *Water Resources Research*, 52(8), 6041-6061.
1399 doi:<https://doi.org/10.1002/2015WR018176>

1400 Reneau, S.L., Katzman, D., Kuyumjian, G.A., Lavine, A., & Malmon, D.V. (2007). Sediment delivery after a
1401 wildfire. *Geology*, 35(2), 151-154. doi:10.1130/G23288A.1

1402 Reynolds, C., (2021). Highway 1 washout near Big Sur expected to be fixed by summer, Los Angeles Times.
1403 [https://www.latimes.com/travel/story/2021-02-25/highway-1-to-big-sur-will-reopen-by-summer-
1404 caltrans-says](https://www.latimes.com/travel/story/2021-02-25/highway-1-to-big-sur-will-reopen-by-summer-caltrans-says)

1405 Robichaud, P., Beyers, J., & Neary, D. (2000). Evaluating the effectiveness of postfire rehabilitation treatments.
1406 *Soil Water Resour Res* 36:103-112 doi:10.1029/1999SW10001

1407 Rosso, R., Rulli, M.C., Bocchiola, D. (2007) Transient catchment hydrology after wildfires in a Mediterranean
1408 basin: runoff, sediment and woody debris *Hydrol Earth Syst Sci* 11:125-140 doi:10.5194/hess-11-125-
1409 2007

1409 Rulli, M.C., & Rosso, R. (2007). Hydrologic response of upland catchments to wildfires. *Advances in Water
1410 Resources*, 30(10), 2072-2086. doi:<https://doi.org/10.1016/j.advwatres.2006.10.012>

1411 Santi, P.M., deWolfe, V.G., Higgins, J.D., Cannon, S.H., & Gartner, J.E. (2008). Sources of debris flow material
1412 in burned areas. *Geomorphology*, 96(3-4), 310-321. doi:10.1016/j.geomorph.2007.02.022

1413 Santi, P.M., & Morandi, L. (2013). Comparison of debris flow volumes from burned and unburned areas.
1414 *Landslides*, 10(6), 757-769.

1415 Schaeffli, B., & Gupta, H. V. (2007). Do Nash values have value? *Hydrological Processes*, 21(15), 2075-2080.
1416 <https://doi.org/10.1002/hyp.6825>

1417 Scheip, C.M., & Wegmann, K.W. (2021). HazMapper: A global open-source natural hazard mapping application
1418 in Google Earth Engine. *Natural Hazards and Earth System Sciences*, 21(5), 1495-1511.

1419 Schönfelder, L. H., Bakken, T. H., Alfredsen, K., & Adera, A. G. (2017). Application of HYPE in Norway.
1420 SINTEF Energi. Rapport.

1421 Scott, D. F., & Van Wyk, D. B. (1990). The effects of wildfire on soil wettability and hydrological behaviour of
1422 an afforested catchment. 121, 239. doi:10.1016/0022-1694(90)90234-o

1423 Scott, D. F. (1993). The hydrological effects of fire in South African mountain catchments. *Journal of hydrology*,
1424 150(2-4), 409-432.

1425 Shakesby, R. A., & Doerr, S. H. (2006). Wildfire as a hydrological and geomorphological agent. *Earth-Science*
1426 *Reviews*, 74(3), 269-307. doi:<https://doi.org/10.1016/j.earscirev.2005.10.006>

1427 Shen H., Lynch, B., Poulsen, C.J., & Yanites, B.J. (2021) A modeling framework (WRF-Landlab) for simulating
1428 orogen-scale climate-erosion coupling *Computers & Geosciences* 146:104625
1429 doi:<https://doi.org/10.1016/j.cageo.2020.104625>

1430 Sidman, G., Guertin, D., Goodrich, D., Unkrich, C., & Burns, I. (2016). Risk assessment of post-wildfire
1431 hydrological response in semiarid basins: the effects of varying rainfall representations in the
1432 KINEROS2/AGWA model. *International Journal of Wildland Fire*, 25, 268-278. doi:10.1071/WF14071

1433 Staley, D. M., Negri, J. A., Kean, J. W., Laber, J. L., Tillery, A. C., & Youberg, A. M. (2016). Updated logistic
1434 regression equations for the calculation of postfire debris flow likelihood in the western United States
1435 (2016-1106). Retrieved from Reston, VA: <http://pubs.er.usgs.gov/publication/ofr20161106>

1436 Staley, D.M., Negri, J.A., Kean, J.W., Laber, J.L., Tillery, A.C., & Youberg, A. M. (2017) Prediction of spatially
1437 explicit rainfall intensity-duration thresholds for post-fire debris-flow generation in the western United
1438 States *Geomorphology* 278:149-162 doi:<https://doi.org/10.1016/j.geomorph.2016.10.019>

1439 Stoof, C.R., Vervoort, R.W., Iwema, J., van den Elsen, E., Ferreira, A.J.D., & Ritsema, C.J. (2012). Hydrological
1440 response of a small catchment burned by experimental fire. *Hydrol. Earth Syst. Sci.*, 16(2), 267-285.
1441 doi:10.5194/hess-16-267-2012

1442 Swain, D.L., Langenbrunner, B., Neelin, J.D., & Hall, A. (2018) Increasing precipitation volatility in twenty-
1443 first-century California. *Nature Climate Change*. 8:427-433 doi:10.1038/s41558-018-0140-y

1444 Swain, D.L. (2021). A Shorter, Sharper Rainy Season Amplifies California Wildfire Risk. *Geophysical Research*
1445 *Letters*, 48(5), e2021GL092843. doi:<https://doi.org/10.1029/2021GL092843>

1446 Tang, H., McGuire, L. A., Rengers, F. K., Kean, J. W., Staley, D. M., & Smith, J. B. (2019a). Developing
1447 and testing physically based triggering thresholds for runoff-generated debris flows. *Geophysical*
1448 *Research Letters*, 46, 8830–8839.
1449 <https://doi.org/10.1029/2019GL083623><https://doi.org/10.1029/2019GL083623>

1450 [Tang, H., McGuire, L. A., Rengers, F. K., Kean, J. W., Staley, D. M., & Smith, J. B. \(2019b\). Evolution of](#)
1451 [debris-flow initiation mechanisms and sediment sources during a sequence of postwildfire rainstorms.](#)
1452 [Journal of Geophysical Research: Earth Surface](#), 124, 1572–1595.
1453 <https://doi.org/10.1029/2018JF004837>

1454 Tognacca, C., Bezzola, G.R., & Minor, H.E. (2000). Threshold criterion for debris-flow initiation due to channel-
1455 bed failure. *Debris-flow hazards mitigation: Mechanics, prediction and assessment* (pp. 89-97).

1456 U.S. Forest Service, Burned Area Emergency Response, Dolan Postfire BAER Soil Burn Severity Map Released,
1457 October 10, 2020, [https://inciweb.nwccg.gov/photos/CALPF/2020-10-06-1821-Dolan-PostFire-](https://inciweb.nwccg.gov/photos/CALPF/2020-10-06-1821-Dolan-PostFire-BAER/related_files/pict20200910-143346-0.pdf)
1458 [BAER/related_files/pict20200910-143346-0.pdf](https://inciweb.nwccg.gov/photos/CALPF/2020-10-06-1821-Dolan-PostFire-BAER/related_files/pict20200910-143346-0.pdf)

1459 U.S. Forest Service, Burned Area Emergency Response, Dolan Fire Burned Area Report, October 13, 2020,
1460 [https://inciweb.nwcg.gov/photos/CALPF/2020-10-06-1821-Dolan-PostFire-](https://inciweb.nwcg.gov/photos/CALPF/2020-10-06-1821-Dolan-PostFire-BAER/related_files/pict20200927-132609-0.pdf)
1461 [BAER/related_files/pict20200927-132609-0.pdf](https://inciweb.nwcg.gov/photos/CALPF/2020-10-06-1821-Dolan-PostFire-BAER/related_files/pict20200927-132609-0.pdf)

1462 U.S. Geological Survey, Postfire Debris flow Hazards: Dolan Fire (Los Padres National Forest, CA), Landslide
1463 Hazards Program, retrieved September 27, 2021, from
1464 https://landslides.usgs.gov/hazards/postfire_debrisflow/detail.php?objectid=312

1465 Vergopolan, N., Chaney, N.W., Beck, H.E., Pan, M., Sheffield, J., Chan, S., & Wood, E.F. (2020). Combining
1466 hyper-resolution land surface modeling with SMAP brightness temperatures to obtain 30-m soil
1467 moisture estimates. *Remote Sensing of Environment*, 242, 111740.
1468 doi:<https://doi.org/10.1016/j.rse.2020.111740>

1469 Wang, J., Wang, C., Rao, V., Orr, A., Yan, E., & Kotamarthi, R. (2019). A parallel workflow implementation
1470 for PEST version 13.6 in high-performance computing for WRF-Hydro version 5.0: a case study over
1471 the midwestern United States. *Geoscientific Model Development*, 12(8), 3523-3539. doi:10.5194/gmd-
1472 12-3523-2019

1473 Williams, A.P., Abatzoglou, J.T., Gershunov, A., Guzman-Morales, J., Bishop, D.A., Balch, J.K., & Lettenmaier,
1474 D.P. (2019). Observed Impacts of Anthropogenic Climate Change on Wildfire in California. *Earth's*
1475 *Future*, 7(8), 892-910. doi:<https://doi.org/10.1029/2019EF001210>

1476 Williams, A.P. et al. (2022) Growing impact of wildfire on western US water supply. 119:e2114069119
1477 doi:10.1073/pnas.2114069119 %J Proceedings of the National Academy of Sciences

1478 Xia, Y., Mitchell, K., Ek, M., Cosgrove, B., Sheffield, J., Luo, L., . . . Lohmann, D. (2012). Continental-scale
1479 water and energy flux analysis and validation for North American Land Data Assimilation System
1480 project phase 2 (NLDAS-2): 2. Validation of model-simulated streamflow. *Journal of Geophysical*
1481 *Research: Atmospheres*, 117(D3). doi:<https://doi.org/10.1029/2011JD016051>

1482 [Young AM, Skelly KT, Cordeira JM \(2017\) High-impact hydrologic events and atmospheric rivers in California: An investigation using the NCEI Storm Events Database *Geophys Res Lett* 44:3393-3401 doi:10.1002/2017GL073077](#)

1483

1484

1485 Yin D., Xue Z. G., Gochis D. J., Yu W., Morales M., & Rafieeiniasab A. (2020) A Process-Based, Fully
1486 Distributed Soil Erosion and Sediment Transport Model for WRF-Hydro 12:1840

1487 Zhang, J. et al. (2011). National Mosaic and Multi-Sensor QPE (NMQ) system: Description, results, and future
1488 plans. *Bull. Amer. Meteor. Soc.*, 92, 1321–1338, <https://doi.org/10.1175/2011BAMS-D-11-00047.1>.

1489 Zhang, J., Qi, Y., Langston, C., Kaney, B., & Howard, K. (2014). A real-time algorithm for merging radar QPEs
1490 with rain gauge observations and orographic precipitation climatology. *J. Hydrometeorol.*, 15, 1794–1809,
1491 <https://doi.org/10.1175/JHM-D-13-0163.1>.

1492 Zhang, J. et al. (2016). Multi-Radar Multi-Sensor (MRMS) quantitative precipitation estimation: Initial
1493 operating capabilities. *Bull. Amer. Meteor. Soc.*, 97, 621–638, [https://doi.org/10.1175/BAMS-D-14-](https://doi.org/10.1175/BAMS-D-14-00174.1)
1494 [00174.1](https://doi.org/10.1175/BAMS-D-14-00174.1).

1495 Zhang S., Zhao, L., Delgado-Tellez, R., Bao, H. (2018) A physics-based probabilistic forecasting model for
1496 rainfall-induced shallow landslides at regional scale *Nat Hazards Earth Syst Sci* 18:969-982
1497 doi:10.5194/nhess-18-969-2018

1498

1499 [Zhu, Y., & Newell, R. E. \(1998\). A Proposed Algorithm for Moisture Fluxes from Atmospheric Rivers. *Monthly Weather Review*, 126\(3\), 725-735. Retrieved May 14, 2022, from \[https://journals.ametsoc.org/view/journals/mwre/126/3/1520-\]\(https://journals.ametsoc.org/view/journals/mwre/126/3/1520-0493_1998_126_0725_apafmf_2.0.co_2.xml\)](#)
1500 [0493_1998_126_0725_apafmf_2.0.co_2.xml](https://journals.ametsoc.org/view/journals/mwre/126/3/1520-0493_1998_126_0725_apafmf_2.0.co_2.xml)
1501
1502
1503

Formatted: Justified, Indent: Left: 0", Hanging: 0.5",
Line spacing: Multiple 1.15 li